وزارة التعليم العالي والبحث العلمي

UNIVERSITE BADJI MOKHTAR
BADJI MOKHTAR UNIVERSITY

جامعة باجي مختار - عنابة

Faculté des Sciences
Département de Physique

Année 2023

THESE

Présentée en vue de l'obtention du diplôme de

DOCTORAT

Radiative association and charge transfer phenomena observed in the argonium gas

Option: Physique Théorique

par

Fatima TALHI

Directeur de thèse: Moncef BOULEDROUA Professeur Université Badji Mokhtar, Annaba

Devant le Jury

Président:	Reda ATTALLAH	Professeur	Université Badji Mokhtar, Annaba
Examinateurs:	Salim HOUAMER	Professeur	Université Ferhat Abbas, Sétif
	Kamel ALIOUA	Professeur	Université Med Cherif Messaadia, Souk Ahras
	Nora LAMOUDI	M.C.A	Université Badji Mokhtar, Annaba

ملخص

العمل المقدم في هذه الأطروحة مخصص لدراسة الظاهرتين الاشعاعيتين الخاصتين بجزيء الأرغونيوم البين نجمي ArH^+ ، الأولى هي ظاهرة الارتباط الاشعاعي، $Ar + H^+ \rightarrow ArH^+$ ، أما الثانية فهي ظاهرة نقل الشحنة الاشعاعي، $Ar^+ + H \rightarrow Ar + H^+$. لأداء كلتا المهمتين، يتم تحديد منحنيات كل من الطاقة الكامنة و عزوم ثنائي القطب من أجل بناء الحالة الأساسية و أول حالتين مثارتين للجزيء ArH^+. بمجرد انشاء جميع المنحنيات المطلوبة و مقارنة خصائصها الفيزيائية و قيمها الطيفية مع البيانات المنشورة في الدراسات السابقة، نقوم بحساب كمي عند قيم طاقوية دنيا وعليا للمقاطع العرضية الخاصة بعملية تكوين الأيون الجزيئي ArH^+ عن طريق الارتباط الاشعاعي، و نقل الشحنة الاشعاعي . أخيرا يتم حساب معاملات المعدل المتعلقة بدرجة الحرارة و تحليلها في مجال درجة الحرارة 1-10000 K.

الكلمات المفتاحية

منحنيات كل من الطاقة الكامنة لجزيء الأرغونيوم، ظاهرة الارتباط الاشعاعي، ظاهرة نقل الشحنة الاشعاعي، معاملات المعدل.

Résumé

le travail présenté dans cette thèse est consacré à l'examen des processus radiatifs de l'argonium interstellaire ArH^+, à savoir, l'association $Ar + H^+ \rightarrow ArH^+$, et le transfert de charge, $Ar^+ + H \rightarrow Ar + H^+$. Pour réaliser ces deux tâches, les courbes d'énergie potentielle et les moments dipolaires correspondants sont déterminés afin de construire l'état fondamental et les deux premiers états excités de l'ArH^+ . Une fois que toutes les courbes requises sont bien établies et que leurs caractéristiques physiques et les valeurs spectroscopiques sont contrastées avec les données publiées précédemment, les sections efficaces, pour les deux processus radiatifs, la formation de l'ion moléculaire ArH^+ par association et transfert de charge sont calculés par mécanique quantique aux énergies inférieures et supérieures. Enfin, les coefficients de taux dépendant de la température sont calculés et analysés dans l'intervale de température $1 - 10000\,\mathrm{K}$.

Mots-clé : les courbes d'énergie potentielle de l'argonium, association radiatif, transfert de charge radiatif, les coefficients de taux de ArH^+

Abstract

The work presented in this thesis is devoted to the examination of the radiative processes of interstellar argonium ArH^+, namely, association, $Ar + H^+ \rightarrow ArH^+$, and charge transfer, $Ar^+ + H \rightarrow Ar + H^+$. To perform both of these tasks, the corresponding potential-energy curves and dipole moments are determined in order to construct the ground and the two first excited ArH^+ molecular states.Once all the required curves are well established and their physical features and spectroscopic values are contrasted with previously published data, the cross sections, for both radiative processes, the formation of the molecular ion ArH^+ by association and charge transfer are computed quantum-mechanically at lower and higher energies. Finally, the temperature-dependent rate coefficients are calculated and analyzed in the temperature range $1 - 10000\,\mathrm{K}$.

Keywords : argonium potential-energy curves, radiative association, radiative charge transfer, ArH^+rate coefficients.

Acknowlegements

First and foremost, I thank the Almighty ALLAH for giving me the strength and patience to work through all these years overcoming many trying moments, so that I have been finally able to accomplish this thesis.

I would like to express my deepest appreciation to my supervisor, Professor **Moncef BOULEDROUA**, from Badji Mokhtar University of Annaba, for his enlightening guidance, without whom none of this work would have been possible. His expertise was invaluable, and I appreciate all the time he has spent helping me achieve this.

I would like to express my gratitude to our jury members who have been so kind to accept to examine my dissertation, Professor **Reda ATTALLAH,** from Badji Mokhtar University of Annaba, Professor **Salim HOUAMER,** from Ferhat Abbas University of Setif, Professor **Kamel ALIOUA,** from Mohamed-Cherif Messaadia University of Souk Ahras, and Dr. **Nora LAMOUDI,** from Badji Mokhtar University of Annaba. Thank you all for devoting a part of your precious time for reading and evaluating this work and for providing helpful comments and remarks.

In addition, this work has been achieved within the framework of the scientific activities of the Radiation Physics Laboratory, RPL at the Physics Department, Badji Mokhtar University of Annaba.

Last but not least, my deepest gratitude goes to my family. I sincerely thank my parents, my two brothers, and my husband for providing me with unfailing support and continuous encouragement throughout my years of study and through the process of researching and writing this thesis. My gratitude for them can hardly be expressed in words, this thesis is dedicated to all of them and especially to my beloved son **Soltan**.

Annaba, May 28^{th}, 2023.

Contents

List of Tables

List of Figures

Introduction

Argonium (ArH^+), the first noble gas molecule discovered in the interstellar medium (ISM), was reported by Barlow [1], who identified two $^{36}ArH^+$ emission lines at 617.525 GHz ($J = 1 \leftarrow 0$) and 1234.603 GHz ($J = 2 \leftarrow 1$) in spectra from the Crab Nebula obtained with the *Herschel Space Observatory,* as illustrated in Fig. 0-1. In addition, Müller *et al* (2013) [2] detected a strong absorption feature at 617.5 GHz, which was initially difficult to identify. After that, Schilke *et al* (2014) [3] pointed out that the unspecified 617.5 GHz line was actually assigned to $^{36}ArH^+$. Moreover, features of $^{38}ArH^+$ were found, which suggested that argonium is prevalent in the ISM. Furthermore, this hydride cation has also been detected in a foreground galaxy by Müller *et al* (2015) [4], they observed the $J = 1 \leftarrow 0$ transition of two argonium's isotopologs, $^{36}ArH^+$ at 617525.23 ± 0.15 MHz ($J = 1 - 0$) and $^{38}ArH^+$ at 616648.76 ± 0.08 MHz ($J = 1 - 0$). These observations yielded an estimation of the argonium presence by the isotopic ratio $^{36}ArH^+/^{38}ArH^+ = 3.46 \pm 0.16$. They concluded that the evolution of this ratio with redshift may constrain nucleosynthetic scenarios in the early universe. Argonium is considered as a good molecular tracer of the almost purely atomic diffuse ISM [4,5]. ArH^+ is primarily formed from the chemical reaction ($Ar^+ + H_2 \rightarrow ArH^+ + H$) [1,5], which is further annihilated by the reaction ($ArH^+ + H_2 \rightarrow Ar + H_3^+$) where the Ar atom is ionized by cosmic rays [3,6].

Rare-gas atoms are stable because of their full-shell configuration. They typically do not form covalent bonds when they interact with each other or other atoms and molecules. At short internuclear distances, the repulsive interaction between the electrons of the full-shell atom is dominant. But at larger internuclear distances, the attractive van der Waals interaction predominates. This interaction arises from the instantaneous and induced multiple moments of the two atoms, leading to the formation of weakly bound van der Waals dimers [7]. The formation of the ArH^+ noble gas molecule was unexpected because we don't normally expect a noble gas atom like argon to form molecules, especially in the harsh environment of a supernova remnant. However, it was realized that there are locations even in

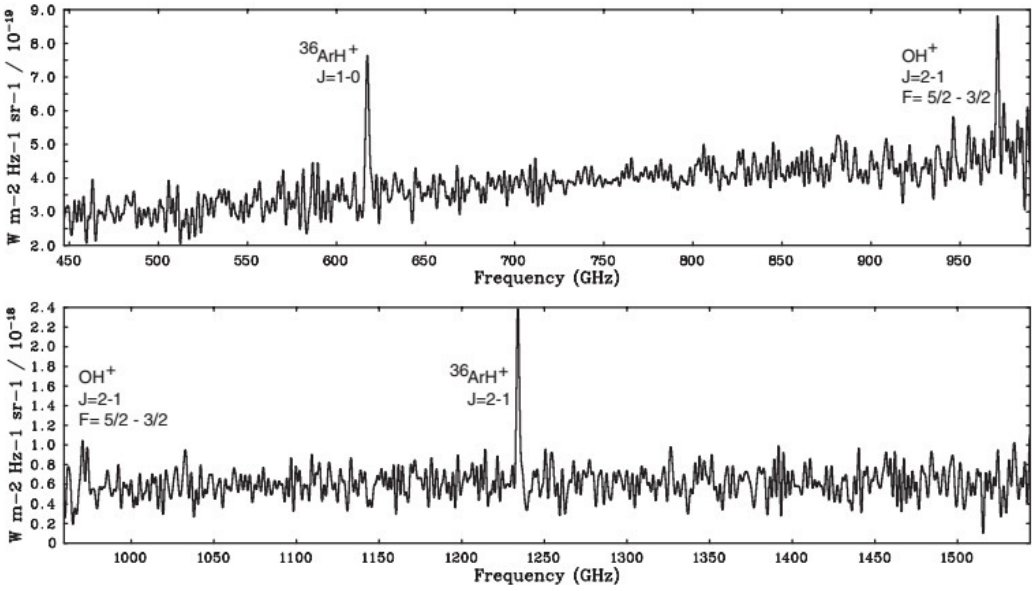

Figure 0-1: The rotational spectrum of ArH^+ from the crab nebula obtained with Herschel space observatory [1].

the Crab Nebula where the circumstances are ideal for a noble gas to react and combine with other elements. There, argon hydride can form and survive in the transition regions between ionized and molecular gases. Hydrides are the first molecules to form because hydrogen is the most common element in the interstellar medium.

It is important to note that the radiative association and radiative charge transfer processes play a crucial role in the formation of molecules in the interstellar medium. In this thesis, the focus is on the theoretical investigation of these processes. It consists of the present introduction, followed by three chapters, and a conclusion. The first Chapter provides a brief introduction to the theory of atom-ion collisions. The second Chapter focuses on constructing potential energy curves, as well as permanent and transition dipole moments. The accuracy of these constructions is evaluated by computing rotational-vibrational levels and radiative lifetimes. Chapter 3 is devided into two parts. The first part addresses the radiative association process of argon atoms and hydrogen ions to form argonium. The quantum mechanical cross sections and the rate coefficients are calculated. The second part is devoted to investigating the radiative charge transfer process. The quantum mechanical cross sections and the rate coefficients are calculated for this process as well. The thesis concludes with a summary of the main results, including comparisions with previously published values where relevant.

Unless otherwise stated, the results are given in atomic units (a.u.).

Chapter 1

Atom-ion collision theory

Collisions between atoms (or ions) A and B can be classified into three main categories [8]. The first category is the *elastic collision*, in which the internal energies of the colliding particles remain unchanged, but the incident paricles are deflected in a specific direction. This type of collision can be represented by the equation

$$\mathrm{A} + \mathrm{B} \rightarrow \mathrm{A} + \mathrm{B}. \tag{1.1}$$

The second category is the *inelastic collision*, where either A or B, or both, are excited to a different energy level. The various possibilities for this type of collision can be expressed as follows

$$\begin{aligned} \mathrm{A} + \mathrm{B} &\rightarrow \mathrm{A}^* + \mathrm{B}, & (1.2)\\ &\rightarrow \mathrm{A} + \mathrm{B}^*, & (1.3)\\ &\rightarrow \mathrm{A}^* + \mathrm{B}^*. & (1.4) \end{aligned}$$

This category includes reactions where one or both species are ionized, resulting in the ejection of one or more electrons and the formation of positive ions

$$\begin{aligned} \mathrm{A} + \mathrm{B} &\rightarrow \mathrm{A} + \mathrm{B}^+ + e^-, & (1.5)\\ &\rightarrow \mathrm{A}^+ + \mathrm{B} + e^-. & (1.6) \end{aligned}$$

The third category is the *charge exchange* which occurs when one or more electrons are transferred between A and B

$$\mathrm{A} + \mathrm{B}^+ \rightarrow \mathrm{A}^+ + \mathrm{B}. \tag{1.7}$$

1.1 Diatomic system

We can express the nonrelativistic Hamiltonian for a diatomic molecule as the sum of five terms

$$H = -\frac{\hbar^2}{2m_A}\nabla^2_{\mathbf{R}_A} - \frac{\hbar^2}{2m_B}\nabla^2_{\mathbf{R}_B} - \frac{\hbar^2}{2m_e}\sum_{i=1}^{N}\nabla^2_{\mathbf{r}_i} + V_e(\mathbf{R}_{A,B}, \mathbf{r}) + V_N(\mathbf{R}_{A,B}), \tag{1.8}$$

where $\hbar$ is the well-known reduced Planck's constant, and m_e, m_A, and m_B denote the electron masse and the nuclei masses of the two species Ar and H, respectively. N refers to the total number of electrons in the system. Additionally, $\mathbf{R}_{A,B}$ represents the position vector of the nuclei relative to a fixed reference, while $\mathbf{r}$ represents the position vector of the electrons relative to the same fixed reference.

The first three terms in this equation (1.8) represent the kinetic energies of the nuclei and electrons. $V_e(\mathbf{R}_{A,B}, \mathbf{r})$ corresponds to the potential energy of the electrons resulting from electron-electron and electron-nucleus interactions. It can be defined as

$$V_e(\mathbf{R}_{A,B}, \mathbf{r}) = -\frac{e^2}{4\pi\varepsilon_0}\left(\sum_{i>j}\frac{1}{|r_i - r_j|} - \sum_{i,I}\frac{Z_I}{|R_I - r_i|}\right). \tag{1.9}$$

On the other hand, $V_N(\mathbf{R}_{A,B})$ represents the potential energy of the nuclei arising from nucleus-nucleus interactions and can be expressed as

$$V_N(\mathbf{R}_{A,B}) = \frac{e^2}{4\pi\varepsilon_0}\frac{Z_A Z_B}{|R_A - R_B|}, \tag{1.10}$$

where Z is the atomic number ($Z_A = Z_{\mathrm{Ar}} = 18, Z_B = Z_{\mathrm{H}} = 1$).

Within the framework of nonrelativistic theory, the elastic collision between the atom A and the ion B^+ is governed by the time-independent Schrödinger equation

$$H\Psi(\mathbf{R}_{A,B}, \mathbf{r}) = E\Psi(\mathbf{R}_{A,B}, \mathbf{r}), \tag{1.11}$$

here, $\Psi(\mathbf{R}_{A,B}, \mathbf{r})$ represents the wave function, and E denotes the total energy of the system. It is important to note that finding an exact solution to equation (1.11) is not feasible,

requiring the use of approximations. In this case, the Born-Oppenheimer approximation is chosen as the preferred approach.

1.2 Born-Oppenheimer approximation

The Born-Oppenheimer approximation is based on the fact that the nuclei have much larger masses than the electrons. Consequently, the wave function of the system $\Psi(\mathbf{R}_{A,B}, \mathbf{r})$ can be expressed as the product of an electronic wave function $\Psi_e(\mathbf{R}_{A,B}, \mathbf{r})$ and a nuclear wave function $\Psi_N(\mathbf{R}_{A,B})$. It is assumed to have the form

$$\Psi(\mathbf{R}_{A,B}, \mathbf{r}) = \Psi_N(\mathbf{R}_{A,B}).\Psi_e(\mathbf{R}_{A,B}, \mathbf{r}), \tag{1.12}$$

here, $\Psi_N(\mathbf{R}_{A,B})$ and $\Psi_e(\mathbf{R}_{A,B}, \mathbf{r})$ represent the nuclear and electronic wave functions, respectively. When solving Schrödinger's equation, we focus solely on the electrons and treat the nuclei as fixed. As a result, our wave functions depend only on the electronic coordinates. The electronic Schrödinger equation can be expressed as

$$H_e\Psi_e(\mathbf{R}_{A,B}, \mathbf{r}) = \left[-\frac{\hbar^2}{2m_e}\sum_{i=1}^{N}\nabla^2_{\mathbf{r}_i} + V_e(\mathbf{R}_{A,B}, \mathbf{r})\right]\Psi_e(\mathbf{R}_{A,B}, \mathbf{r}) = E_e(\mathbf{R}_{A,B}).\Psi_e(\mathbf{R}_{A,B}, \mathbf{r}). \tag{1.13}$$

This equation represents the behavior of the electronic system.

The Schrödinger equation (1.11), which includes both the electronic and nuclear components, can be expressed as

$$H\Psi(\mathbf{R}_{A,B}, \mathbf{r}) = \left[-\frac{\hbar^2}{2m_A}\nabla^2_{\mathbf{R}_A} - \frac{\hbar^2}{2m_B}\nabla^2_{\mathbf{R}_B} + H_e + V_N(\mathbf{R}_{A,B})\right]\Psi(\mathbf{R}_{A,B}, \mathbf{r}) = E_T\Psi(\mathbf{R}_{A,B}, \mathbf{r}). \tag{1.14}$$

By using the relationship (1.12) , we get

$$\left[-\frac{\hbar^2}{2m_A}\nabla^2_{\mathbf{R}_A} - \frac{\hbar^2}{2m_B}\nabla^2_{\mathbf{R}_B} + E_e + V_N(\mathbf{R}_{A,B})\right]\Psi_N(\mathbf{R}_{A,B}, \mathbf{r}) = E_T\Psi_N(\mathbf{R}_{A,B}). \tag{1.15}$$

This represents the nuclear Schrödinger equation, which describes the dynamics of the nuclei in the system. It can be written as

$$\left[-\frac{\hbar^2}{2m_A}\nabla^2_{\mathbf{R}_A} - \frac{\hbar^2}{2m_B}\nabla^2_{\mathbf{R}_B} + V(\mathbf{R}_{A,B})\right]\Psi_N(\mathbf{R}_{A,B}, \mathbf{r}) = E_T\Psi_N(\mathbf{R}_{A,B}), \tag{1.16}$$

where $V(\mathbf{R}_{A,B}) = V_N(\mathbf{R}_{A,B}) + E_e$ is known as the full internuclear potential for each electronic state.

In order to simplify our problem, it is convenient to move from the laboratory coordinates to the center of mass coordinates. The centre of mass position vector, denoted as $\boldsymbol{\rho}$ is given by

$$\boldsymbol{\rho} = \frac{m_A \mathbf{R}_A + m_B \mathbf{R}_B}{m_A + m_B}, \tag{1.17}$$

where the reduced mass of the system is defined as

$$\mu = \frac{m_A m_B}{m_A + m_B}. \tag{1.18}$$

The relative vector between the two nuclei is $\mathbf{R} = \mathbf{R}_A - \mathbf{R}_B$. Using these coordinates, the equation (1.16) can be written as

$$\left[-\frac{\hbar^2}{2(m_A + m_B)} \nabla^2_{\boldsymbol{\rho}} - \frac{\hbar^2}{2\mu} \nabla^2_{\mathbf{R}} + V(\mathbf{R}) \right] \Psi_N(\boldsymbol{\rho}, \mathbf{R}) = E_T \Psi_N(\boldsymbol{\rho}, \mathbf{R}). \tag{1.19}$$

It is worth noting that the first term represents the kinetic energy of the center of mass. Since it does not affect the relative movement of the two atoms, it can be neglected in this context.

By putting $\mathbf{R} = \mathbf{R}_A - \mathbf{R}_B$, the collision between the two species can be described by the equation

$$\left[\frac{-\hbar^2}{2\mu} \nabla^2_{\mathbf{R}} + V(\mathbf{R}) \right] \Psi_N(\mathbf{R}) = E \Psi_N(\mathbf{R}), \tag{1.20}$$

here, $E = E_T - E_\rho$, where E_ρ represents the centre of masse energy. Thus, according to this equation, the study of the collision between the two species is reduced to investigating the diffusion of a single particle by a potential. The resolution of this equation will allow us to determine the wave functions of the initial and final states. In fact, the electronic schrödinger equation (1.13) is solved using approximations at different values of R to obtain the wave functions $\Psi_e(\mathbf{R}_{A,B}, \mathbf{r})$ and potential energies $V_e(\mathbf{R})$.

The potential energies can be graphed as illustrated in Fig. 1-1. This graph shows the potential energy of a diatomic molecule as a function of internuclear separation, representing the potential energy function for the nuclei. When R is significantly large, the two species exhibit weak interaction. As R decreases, the interaction becomes stronger, resulting in a substantial negative energy value, indicating the formation of a bond between the two species. At very small values of R , the internuclear repulsion becomes subtantial, leading to a large

positive energy. This energy function governs the motion of the nuclei.

We represent schematically in Fig. 1-2 the Born-Oppenheimer potential energy curves for a ground and an excited electronic state of a diatomic molecule. To differentiate between the states, the notation of a single prime ($\prime$) is used for the upper states (excited states), while a double prime ($\prime\prime$) is used for the lower states (ground state). The vibronic energy level structure of a diatomic molecule can be described by the following ralations [9, 10].

$$\tilde{v}_{v'v''} = T_e + G_{v'} - G_{v''}, \tag{1.21}$$

$$T_e = \tilde{v}_{00} + G_{v''=0} - G_{v'=0}. \tag{1.22}$$

In these equations, T stands for the electronic energy (the subscript $'e'$ for "equilibrium" indicates that the energy difference is between the minima of the excited and ground electronic state potential-energy functions), and G represents the vibrational energy of the ground and excited electronic states. The transition wave number between an initial $v\prime$ and a final v'' vibrational level can be derived by substituting equation (1.22) into equation (1.21), resulting in

$$\tilde{v}_{v'v''} = \tilde{v}_{00} + G_{v''=0} - G_{v'=0} + G_{v'} - G_{v''}. \tag{1.23}$$

By approximating the vibrational motion as a Morse oscillator [9], the vibrational energy in the excited electronic state $G_{v'}$ can be approximated as

$$G_{v'} \simeq \omega'_e \left(v' + \frac{1}{2}\right) - \omega_e x'_e \left(v' + \frac{1}{2}\right)^2. \tag{1.24}$$

Considering only transitions to the ground vibronic state, the equation (1.23) can be written as

$$\tilde{v}_{v'v''=0} = \tilde{v}_{00} + \omega'_e \left(v' + \frac{1}{2}\right) - \omega_e x'_e \left(v' + \frac{1}{2}\right)^2 - \left(\frac{\omega'_e}{2} - \frac{\omega_e x'_e}{4}\right). \tag{1.25}$$

where, ω_e and $\omega_e x_e$ represent the harmonic and anharmonic vibrational constants, respectively.

The dissociation energies D_0 and D_e are defined with respect to the ground vibrational state and the minimum of the potential-energy function of an electronic state. They can be expressed as follows

$$D'_0 = D''_0 + \tilde{v}_{atom} - \tilde{v}_{00}, \tag{1.26}$$

$$D''_0 = D''_0 + G_{v''=0}. \tag{1.27}$$

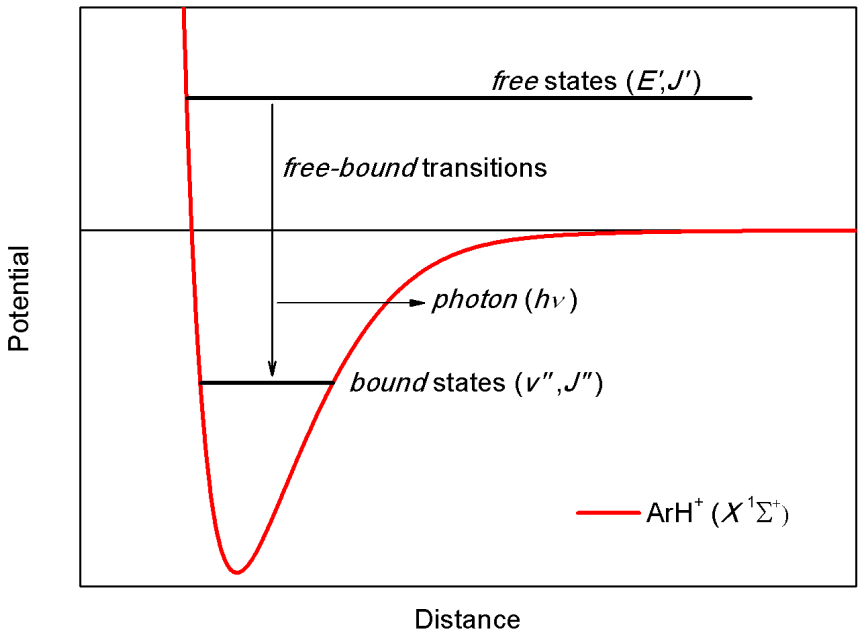

Figure 1-1: Schematic potential energy curve of the ground state of a diatomic molecule.

To account for the influence of vibrational motion on the rotational and centrifugal distortion constants, we express the rotational distortion constants of a vibrational level v as a power series expansion in $(v + 1/2)$. For the rotational distortion constants, we have

$$B_v = B_e - \alpha_e \left(v + \frac{1}{2} \right) + \gamma_e \left(v + \frac{1}{2} \right)^2 + ..., \tag{1.28}$$

Similarly, for the centrifugal distortion constants, we have

$$D_v = D_e - \beta_e \left(v + \frac{1}{2} \right), \tag{1.29}$$

In these equations, B_e and D_e represent the values of the rotational and centrifugal constants at the equilibrium position. On the other hand, B_v and D_v represent the rotational and centrifugal distortion constants specific to the vibrational level v.

1.3 Wave functions

In order to solve equation (1.20), we suppose that the potential is central $V(R)$ i.e. the potential energy of the molecule depends only on its distance from the origin R (the module of the position vector $R = |\mathbf{R}|$). We express the new wave function as a product of two

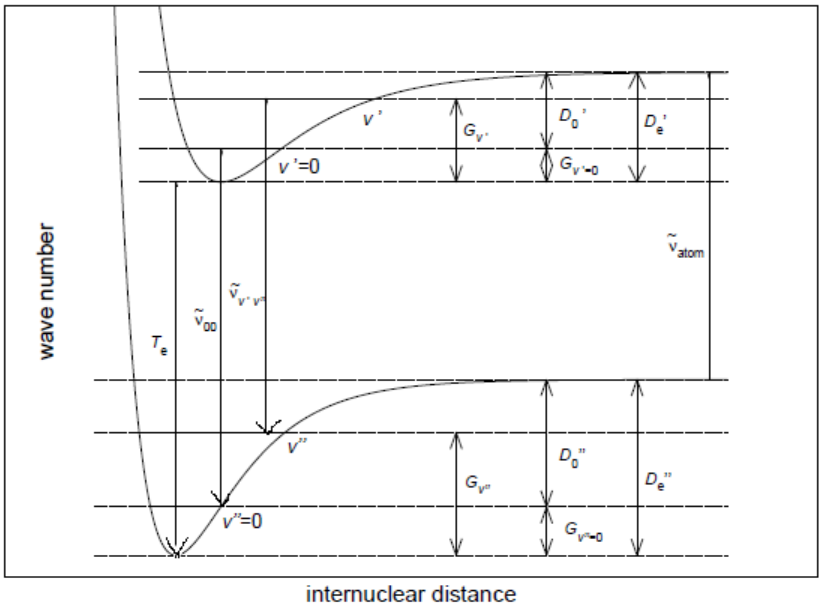

Figure 1-2: Schematic potential energy curves of the ground and excited electronic states of a diatomic molecule.

functions: a purely radial function $\Phi_J(R)$ related to the relative motion of the nuclei, and a spherical harmonic $Y_J^m(\theta, \phi)$ associated with their rotation

$$\Psi_N(\mathbf{R}) = \frac{\Phi_J(R)}{R} Y_J^m(\theta, \phi), \tag{1.30}$$

where θ and ϕ denote the polar and azimuthal angles, respectively. The spherical harmonics are eigenfunctions of the operators $\mathbf{J}^2$ and J_z (the projection of the angular momentum $\mathbf{J}$ on the z-axis)

$$\mathbf{J}^2 Y_J^m(\theta, \phi) = J(J+1)\hbar^2 Y_l^m(\theta, \phi), \tag{1.31}$$

$$J_z Y_l^m(\theta, \phi) = m\hbar^2 Y_l^m(\theta, \phi). \tag{1.32}$$

It is convenient to use spherical coordinates

$$\nabla_R^2 = \frac{1}{R^2}\frac{\partial}{\partial R}(R^2 \frac{\partial}{\partial R}) - \frac{J^2}{\hbar^2 R}. \tag{1.33}$$

The equation (1.20) becomes

$$-\frac{\hbar^2}{2\mu}\frac{d^2\Phi_J(R)}{dR^2} + \left[\frac{\hbar^2}{2\mu}\frac{J(J+1)}{R^2} + V(R)\right]\Phi_J(R) = E\Phi_J(R), \tag{1.34}$$

$$\frac{d^2\Phi_J(R)}{dR^2} + \frac{2\mu}{\hbar^2}\left[E - \left(\frac{\hbar^2}{2\mu}\frac{J(J+1)}{R^2} + V(R)\right)\right]\Phi_J(R) = 0. \tag{1.35}$$

This equation is similar to the *one dimensional* Schrödinger equation, except that the potential is replaced by an effective potential

$$V_{eff}(R) = -\frac{\hbar^2}{2\mu}\frac{J(J+1)}{R^2} + V(R), \tag{1.36}$$

for $J \neq 0$, the first term in the effective potential represents a *centrifugal barrier* that tends to push the molecule away from the force center. The solutions of the radial wave equation (1.34) are the radial wave functions. This solution depends on the sign of the energy E. Thus, For $E < 0$, the system forms a quasi-molecule, and the energy quantum states are called *bound states*. We denote their wave functions as $\Phi_J(R) = \Phi_{v,J,\Lambda}(R)$. On the other hand, for $E > 0$, the system belongs to a continuum of energy $E = \epsilon$, and the energy quantum states in this case are called *free states.* Their wave functions can be denoted as $\Phi_J(R) = \Phi_{\epsilon,J,\Lambda}(R)$.

1.4 Molecular states and allowed transitions

The total angular momentum is given by $J = L + S$, where L represents the azimuthal quantum number and S represents the spin quantum number. In the case of a diatomic molecule, the quantum state is denoted as ${}^{2S+1}\Lambda^{\pm}$, where $(2S + 1)$ is the multiplicity of the molecular state. The plus sign $(+)$ indicates that the electronic wave function remains unchanged under reflection. Conversely, if it changes, we use the minus sign $(-)$. Λ represents the absolute value of M_L, which corresponds to the projection of L, where $M_l = 0 \pm 1, \pm 2$, ..., $\pm L$ and

$$\Lambda = |M_l| = \left\{ \begin{array}{c} 0 \Longleftrightarrow \Sigma \\ 1 \Longleftrightarrow \Pi \\ 2 \Longleftrightarrow \Delta \\ . \\ . \\ . \\ |L| \end{array} \right\}.$$

The electronic states of diatomic molecules are denoted by letters

- X denotes the ground state.
- A,B,C,..... represent the excited states with the same multiplicity as the ground state.
- a,b,c,..... represent the excited states with a different multiplicity from the ground state.

Not all transitions between molecular states are allowed. There are selection rules or transition rules that constrain the possible transitions between quantum states. These rules are as follows:

- $\Delta J = 0, \pm 1$, except for transitions where both initial and final states have $J = 0$.
- $\Delta S = 0$, allowing transitions between states with the same multiplicity.
- $\Delta \Lambda = 0, \pm 1$.
- The molecular states involved in the transition should have the same sign.

  These selection rules determine which transitions are permitted between different molecular states.

Chapter 2

Theoretical study of argon hydrid

In this chapter, we present in detail the method of construction of the potential energy curves $V(R)$ for the ground and excited states of ArH^+. Then, we explain the adapted method for the construction of the permanent and transition dipole moments, which connect the ground and excited molecular states of the ArH^+ cation. Finally, we aim to assess the quality of our constructed potentials as well as the permanent and transition dipole moments by calculating rotational-vibrational levels and radiative lifetimes.

2.1 Potential energy curves

The information provided by the ion-atom interaction potential is used in the theoretical calculations and interpretations of the majority of phenomena involving ions in atomic gases. However, the potential energy curves for the electronic excited states can exhibit a wide range of shapes. These curves can be strongly bound, very shallow, or even entirely repulsive. Additionally, they can display multiple potential wells.

2.1.1 ArH^+ systems

At thermodynamic equilibrium, when an argon atom in its ground state $Ar(^1S)$ interacts with a hydrogen ion H^+, the two species approach each other through the ground state $X^1\Sigma^+$, as described by equation (2.1). Whereas, they rather form a quasi molecule in one of the four $C^1\Sigma^+$, $D^1\Pi, c^3\Sigma^+$ and $d^3\Pi$ excited molecular states when the argon atom is in the first excited state $Ar(^{1,3}P)$ and interacts with hydrogen ion H^+, as shown in equation (2.2). However, a quasi molecular system is formed when an argon ion $Ar^+(^2P)$ and hydrogen atom $H(^2S)$ interact mutually along one of the four possible molecular symetries, namely, $A^1\Sigma^+$,

$B^1\Pi$, $a^3\Sigma^+$, and $b^3\Pi$, as depicted in equation (2.3).

$$\mathrm{Ar}(^1S) + \mathrm{H}^+ \longrightarrow \mathrm{ArH}^+(X^1\Sigma^+), \tag{2.1}$$

$$\mathrm{Ar}^+(^2P) + \mathrm{H}(^2S) \longrightarrow \mathrm{ArH}^+ \left\{ \begin{array}{c} A^1\Sigma^+ \\ B^1\Pi \\ a^3\Sigma^+ \\ b^3\Pi \end{array} \right\}, \tag{2.2}$$

$$\mathrm{Ar}(^{1,3}P) + \mathrm{H}^+ \longrightarrow \mathrm{ArH}^+ \left\{ \begin{array}{c} C^1\Sigma^+ \\ D^1\Pi \\ c^3\Sigma^+ \\ d^3\Pi \end{array} \right\}. \tag{2.3}$$

In the present study, our focus is on the singlet molecular states $X^1\Sigma^+$, $A^1\Sigma^+$, $B^1\Pi$, $C^1\Sigma^+$ and $D^1\Pi$, as transitions occur between the states of the same parity.

2.1.2 Potential construction

The interaction potentials $V(R)$ used in the required calculations do not have an accurate analytical form. Instead, they are constructed in three internuclear separation domains:

- short region $0 \leq R \leq R_s$;
- intermediate region $R_s \leq R \leq R_l$;
- long region $R_l \leq R \leq \infty$.

Here, R_s and R_l denote respectively the internuclear distances of the first and last known points of the intermediate region. To ensure a smooth and appropriate connection between these three regions, the *cubic spline* numerical interpolation method is employed. This method is known to be highly effective for handling such curve constructions [11].

Short region

In this region, where $0 \leq R \leq R_s$, the forces are generally repulsive. They are mainly due to the overlapping of the electron clouds of the two species and occur especially when they are sufficiently close together. When the distance between their nuclei decreases, the interaction

Table 2.1: Short-range constant parameters (in a.u.) that appear in the Born-Meyer potentials (2.4).

Molecular	Short range	
state	α	β
$X\,^1\Sigma^+$	62.35	3.635
$A\,^1\Sigma^+$	59.77	3.419
$B\,^1\Pi$	60.55	3.456
$C\,^1\Sigma^+$	61.06	3.527
$D\,^1\Pi$	61.48	3.548

potential experiences a substantial increase. To describe this repulsive interaction potential, a simple and approximate formula known as the Born-Mayer potential [12] is employed

$$V_{SR} = \alpha \exp(-\beta R), \tag{2.4}$$

where α and β are the Born-Mayer constant parameters that need to be determined for each molecular state of ArH^+. Assuming that the potential $V\ (R)$ and its first derivatives are continuous and well-known at $R = R_s$, the following relationships allow us to compute these parameters

$$\alpha = V(R_s) \exp(+\beta R_s), \tag{2.5}$$

and

$$\beta = \frac{-1}{V(R_s)} \left(\frac{dV(R)}{dR} \right)_{R=R_s}. \tag{2.6}$$

The derivative of $V(R)$ at $R = R_s$ is determined numerically using the *cubic spline* method. The computed values of α and β are listed in Table 2.1.

Long region

In this region, namely for $R_l \leq R \leq \infty$, the potential is generally attractive due to the interactions between the electric dipole moments. At long distances, when the electronic overlap is negligible, there are three contributions to these interaction forces: electrostatic, inductive, and dispersive. The potential here can be expanded into a series of inverse powers, also known as the van der Walls potential given by the relationship

$$V_{LR}(R) \backsim -\sum_n \frac{C_n}{R^n}, \tag{2.7}$$

Table 2.2: Compilation of the static multipolar polarizabilities of ground hydrogen and argon (in a.u.). The adopted quadrupolar and octupolar polarizabilities are marked with $*$.

System	C_{d}	C_{q}	C_{o}	Refs.
Ar^+ in H	4.50	15.0*	131.25*	[17]
	4.475	14.93	130.8	[19]
H^+ in Ar	11.062	51.862	536.38	[20]
	11.143	51.844	534.85	[21]
	11.08	52.80*	536.4*	[18]

*the adopted *quadrupolar* and *octupolar* polarizabilities.

where C_n are the dispersion coefficients. It is important to note that this analytical form is applicable for distances greater than a specific value, denoted as R_{LR} called the Le Roy radius. For the purpose of our work, we will consider the first three coefficients, thus the relationship becomes

$$V_{LR}(R) = -\left(\frac{C_4}{R^4} + \frac{C_6}{R^6} + \frac{C_8}{R^8}\right), \tag{2.8}$$

with $C_4 = \frac{1}{2}C_d, C_6 = \frac{1}{2}C_q$, $C_8 = \frac{1}{2}C_o$, are the usual dispersion coefficients which are the halves of the static electric dipolar C_d, quadrupolar C_q, and octupolar C_o polarisabilities of the involved neutral species, namely, H or Ar. For the dipole polarizability, we have adopted the values proposed by NIST, i.e., $C_d = 4.50$ for hydrogen and $C_d = 11.23$ for argon [13]. Both data can be compared to the recommended values 4.50456 ± 0.00003 and 11.083 ± 0.007 from Schwerdtfeger and Nagle [14] and with the measured values $C_d = 4.49974$ of Miller and Bederson [15] and $C_d = 11.22923$ of Olney *et al* [16], respectively. The adopted values of the quadrupole and octupole polarizabilities are taken from references [17, 18], some further published polarizabilities and the adopted values are assembled in Table 2.2.

Intermediate region

The internuclear distance in this case is in the range $R_s \leq R \leq R_l$. The interactions between atoms and ions are predominantly electrostatic and obey Coulomb's law. This region plays a fundamental role in constructing the potential energy curves for the other two regions. The potential energy curves were constructed using *ab-initio* points generated by Stolyarov at internuclear distances ranging from 0.5 to $12a_0$, where a_0 represents the Bohr radius. Some of the *ab-initio* values are listed in Table 2.3. The ab-initio points offer valuable insights into the behavior and characteristics of the system within the intermediate region. They serve as a crucial basis for constructing precise representations of the interaction potential in this

Table 2.3: Some values of *ab-initio* points (in a.u.), for the singulet states of the ArH^+ system.

Distance	States				
R (a.u.)	$X\ ^1\Sigma^+$	$A\ ^1\Sigma^+$	$B\ ^1\Pi$	$C\ ^1\Sigma^+$	$D\ ^1\Pi$
0.5	−516.921551	−516.163823	−516.223564	−516.151357	−516.191782
1.0	−525.210143	−524.506963	−524.609518	−524.453330	−524.542299
1.5	−526.834249	−526.150607	−526.235250	−526.101875	−526.211267
2.0	−527.164648	−526.507328	−526.655238	−526.496111	−526.552823
2.5	−527.203576	−526.650895	−526.817874	−526.579155	−526.605272
3.0	−527.177808	−526.756736	−526.898801	−526.577737	−526.594728
3.5	−527.143584	−526.837830	−526.941923	−526.569025	−526.578546
4.0	−527.114011	−526.895448	−526.963921	−526.566861	−526.568371
4.5	−527.091457	−526.933058	−526.974405	−526.570382	−526.565578
5.0	−527.075603	−526.955967	−526.978971	−526.575882	−526.569747
5.5	−527.065341	−526.968908	−526.980697	−526.581070	−526.579238
6.0	−527.059226	−526.975574	−526.981171	−526.587381	−526.590384
6.5	−527.055793	−526.978668	−526.981157	−526.598783	−526.600063
7.0	−527.053896	−526.979947	−526.980990	−526.607610	−526.607286
7.5	−527.052820	−526.980395	−526.980803	−526.613915	−526.612378
8.0	−527.052173	−526.980500	−526.980640	−526.618387	−526.616173
8.5	−527.051759	−526.980479	−526.980510	−526.621725	−526.619357
9.0	−527.051477	−526.980421	−526.980409	−526.624107	−526.621886
10.0	−527.051120	−526.980300	−526.980266	−526.625408	−526.623505
12.0	−527.050784	−526.980138	−526.980101	−526.621480	−526.619709

region.

2.1.3 PEC's representation and caracterisation

The constructed ArH^+ potential energy curves of the five molecular states $X^1\Sigma^+$, $A^1\Sigma^+$, $B^1\Pi$, $C^1\Sigma^+$, and $D^1\Pi$ are shown in Fig. 2-1. These curves can be characterized by some spectroscopic constants, such as dissociation energy (potential well-depth) D_e, the equilibrium distance R_e, and the hump h. We determined these parameters for each symmetry using our constructed curves and all the results are gathered in Table 2.4 and compared with the previous published data when available.

- $Ar(^1S) + H^+$ interaction

  The ground state $X^1\Sigma^+$ has a very shallow well. Its depth is found to be $D_e = 33\,779.3\,cm^{-1}$, corresponding to an equilibrium distance of $R_e = 1.277$ Å. These results are in excellent agreement with the values $D_e = 33\,391.36\,cm^{-1}$ and $R_e = 1.279$ Å of Stolyarov and Child [22].

- $Ar(^{1,3}P) + H^+$ interaction

Table 2.4: Spectroscopic data of the constructed ArH^+ potentials.

Molecular state	Equilibrium distance R_e (Å)	Well depth $-D_e$ (cm^{-1})	Hump h (cm^{-1})	Refs.
$X\,^1\Sigma^+$	1.277	33 779.3		
	1.279	33 391.36		[22]
	1.268	34 608.4		[23]
	1.286	31 374.97		[24]
	1.244 ± 0.003	$33\,375.37 \pm 432.77$		[25]
	1.280	32 460		[26]
$A\,^1\Sigma^+$	4.286	31.0457		
$B\,^1\Pi$	3.285	192.049		
$C\,^1\Sigma^+$	5.172	761.211	123.708	
$D\,^1\Pi$	5.204	722.278	123.706	

The first excited states $A^1\Sigma^+$ and $B^1\Pi$ are both found to be repulsive. The well-depth of the $A^1\Sigma^+$ state is $D_e = 31.0457\,cm^{-1}$, and for the $B^1\Pi$ state it is $D_e = 192.049\,cm^{-1}$, with equilibrium distances of $R_e = 4.286\,Å$ and $R_e = 3.285\,Å$, respectively.

- $Ar^+(^2P) + H(^2S)$ interaction

  The second excited states $C^1\Sigma^+$ and $D^1\Pi$ are metastable, exhibiting shallow local minima at $R \approx 2.55 - 2.65a_0$. The well-depth of the $C^1\Sigma^+$ state is $D_e = 761.211\,cm^{-1}$, and for the $D^1\Pi$ state it is $D_e = 722.278\,cm^{-1}$. The equilibrium distances for these states are $R_e = 5.172\,Å$ and $R_e = 5.204\,Å$, respectively. Additionally, we note the presence of humps at $h = 123.708\,cm^{-1}$ and $h = 123.706\,cm^{-1}$ for the $C^1\Sigma^+$ and $D^1\Pi$ states, respectively, both located at $R = 11.95a_0$.

2.2 Permanent and transition dipole moments

The dipole moment as a function of internuclear distance describes the intramolecular electronic charge distribution at different bond lengths and provides information on the changes in the corresponding electronic structure.

2.2.1 Dipole moment's construction

To be able to perform the required numerical calculations, we also need the permanent dipole moment (PDM) $d(R)$ and the transition dipole moments (TDMs) $D(R)$ which connect the lower electronic state to the upper state. They are constructed with a similar numerical

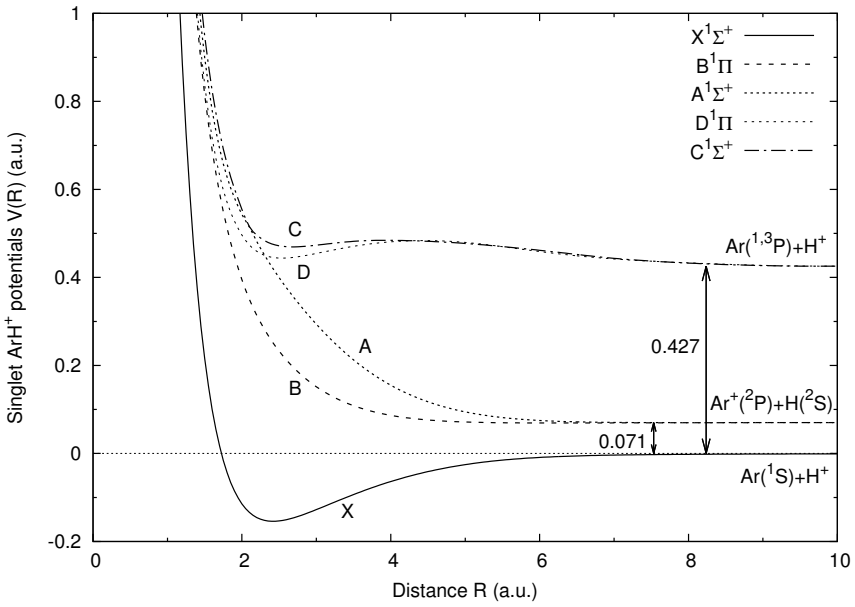

Figure 2-1: ArH^+ potential-energy curves, as constructed from the Stolyarov and Child data points [22].

procedure to that reported previously for potential energy curves. Therefore, we adopted over the internuclear interval $0 \leq R \leq 12$ the calculated *ab-initio* data points computed by Stolyarov and Child [22]. Some values of these data are listed in Table 2.5

- **For free-bound transitions:** $(X^1\Sigma^+ \rightarrow X^1\Sigma^+)$

  The permanent dipole moment (PDM) data points are connected to the linear form at short range,

  $$d(R) = a + bR, \tag{2.9}$$

  where a and b are two constants $(a = 0.1123, b = -0.5785)$ and to the formula at long range

  $$d(R) = \frac{R}{2} - \frac{2C_d}{R^2}. \tag{2.10}$$

- **For free-bound transitions** $(A \rightarrow X,\ B \rightarrow X,\ C \rightarrow X$ and $D \rightarrow X)$.

  In this case, for long distances, the transition dipole moments data points are connected to the formula

  $$D(R) = D_\infty + \frac{A}{R^n}. \tag{2.11}$$

  This formula has been proposed by Chu and Dalgarno [27], where A is a constant parameter and D_∞ is the asymptotic value of $D(R)$, in order to obtain their values, we

Table 2.5: Some values of the *ab initio* points of the transition dipole moments, used for the constructions of the singulet states of the system ArH^+.

Distance	States			
R(a.u.)	$A\ ^1\Sigma^+ \leftarrow X\ ^1\Sigma^+$	$B\ ^1\Pi \leftarrow X\ ^1\Sigma^+$	$C\ ^1\Sigma^+ \leftarrow X\ ^1\Sigma^+$	$D^1\Pi \leftarrow X\ ^1\Sigma^+$
1.5	0.000	0.412	−1.024	0.781
2.0	0.000	−0.071	−0.044	0.857
2.5	0.868	−0.088	0.000	0.870
3.0	1.304	−0.100	0.000	0.880
3.5	1.528	−0.105	0.000	0.873
4.0	1.685	−0.103	0.000	0.851
4.5	1.785	−0.099	0.000	0.836
5.0	1.784	−0.085	0.000	0.877
5.5	1.646	−0.071	0.015	0.901
6.0	1.386	−0.057	0.945	0.846
6.5	1.079	−0.044	1.335	0.782
7.0	0.794	−0.033	1.421	0.730
7.5	0.563	−0.023	1.375	0.684
8.0	0.391	−0.017	1.368	0.646
8.5	0.267	−0.011	1.120	0.604
9.0	0.180	−0.008	0.800	0.566
10.0	0.080	−0.004	0.609	0.505
12.0	0.015	−0.001	0.465	0.421

have fitted our computed long-range TDM data points to a form similar to the previous equation. For the $\Sigma - \Sigma$ transitions our fitting yields $D_\infty = 0.385901$, $A = 916671$, $n = 6.60108$ and for the $\Sigma - \Pi$ transitions, $D_\infty = 0.15619$, $A = 11.5651$, $n = 1.52006$.

In the short-range region, the transition dipole moments $D(R)$ follow the linear form

$$D(R) = p + qR, \tag{2.12}$$

where p and q are two parameters determined by the continuity conditions of the $D(R)$ function. We have found for the $A \rightarrow X$ transition ($p = 4.8704$, $q = -6.4772$), for the $B \rightarrow X$ transition ($p = 0.6712$, $q = -3.9785$), for the $C \rightarrow X$ transition ($p = -0.4811$, $q = -0.1084$), and for the $D \rightarrow X$ transition ($p = 1.2099$, $q = 0.5490$).

2.3 PECs and TDMs assessments

We assess the quality and accuracy of the constructed PECs and TDMs by calculating the rotational-virational energy levels and their radiative lifetimes.

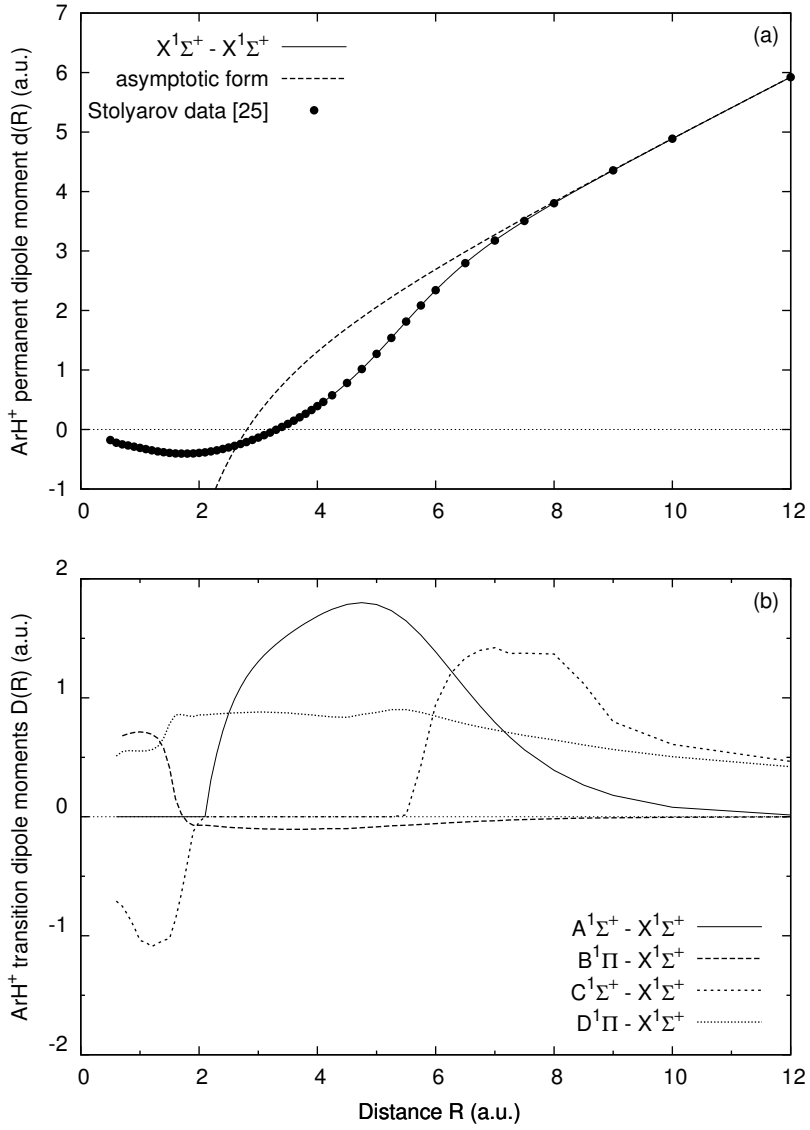

Figure 2-2: (a) The ArH^+ PDM relative to $X - X$ transition. (b) ArH^+ TDMs in connection with the $X \leftarrow A$, $X \leftarrow B$, $X \leftarrow C$, and $X \leftarrow D$ transitions.

2.3.1 Ro-vibrational energy levels

Calculating the rotational vibrational states is one of the methods used to assess the precision of the potentials we have constructed. The ro-vibrational energy $E(v, J) = E_{v,J}$ of a dimer is characterized by v and J, which are the vibrational and rotational quantum numbers, respectively. This energy is easily obtained by solving numerically the radial wave equation (1.34) which rewritten as

$$-\frac{\hbar^2}{2\mu}\frac{d^2}{dR^2}\Phi_{v,J}(R) + \left[\left(\frac{\hbar^2}{2\mu}\frac{J(J+1)}{R^2} + V(R)\right)\right]\Phi_{v,J}(R) = E_{v,J}\Phi_{v,J}(R). \tag{2.13}$$

In the case when a diatom is rotating and vibrating at the same time, the rovibrational energy can be presented by the sum of two terms

$$E(v, J) = G(v, J = 0) + F_v(J), \tag{2.14}$$

where $G(v, J = 0)$ is the vibrational energy affected by vibration, it is expressed in terms of $J(J + 1)$ power as follow [28]

$$F_v(J) = B_v J(J + 1) - D_v.\left[J(J + 1)\right]^2 + H_v\left[J(J + 1)\right]^3 + ... \tag{2.15}$$

where B_v is the v-dependent effective rotation constant associated with each vibrational level. D_v and H_v are the *centrifugal distortion* constants.

Rotationless levels

In the case of bound states, the potential $V(R)$ exhibits a minimum at the equilibrium distance R_e, which is defined by $V(R_e) = -D_e$. In this case, the potential can be expanded in a power series of $(R - R_e)$ around $(R = R_e)$, yields,

$$V(R) = -D_e + (R - R_e)\left(\frac{dV(R)}{dR}\right)_{R=R_e} + \frac{1}{2}(R - R_e)^2\left(\frac{d^2V(R)}{dR^2}\right)_{R=R_e} + ... \tag{2.16}$$

Considering that we truncate the expansion at the second order, we obtain,

$$V(R) = -D_e + \frac{1}{2}k(R - R_e)^2, \tag{2.17}$$

where $k = \left(\frac{d^2V(R)}{dR^2}\right)_{R=R_e}$. If the rotation of the diatom is negligible, the purely radial equation (2.13) simplifies to that of a harmonic oscillator, and the vibrational energy can be expressed as [29]

$$G_{vib} = G(v, J = 0) = \hbar\omega_e \left(v + \frac{1}{2}\right), \tag{2.18}$$

where

$$\omega_e = \sqrt{\frac{k}{\mu}} \tag{2.19}$$

is the vibrational pulsation. In the harmonic oscillator approximation, the vibrational levels are equidistant. However, for real molecules, the energy levels are not equally spaced due to the anharmonicity of the potential curve. The highest levels are closer to each other, and the vibrational energy in this case is best described by a series in power of $\left(v + \frac{1}{2}\right)$

$$G_{vib} = \hbar\omega_e \left(v + \frac{1}{2}\right) - \omega_e x_e \left(v + \frac{1}{2}\right)^2 + \omega_e y_e \left(v + \frac{1}{2}\right)^3 + ... \tag{2.20}$$

with $\omega_e x_e$ and $\omega_e y_e$ are the first anharmonicity coefficients [30].

Vibrationless levels

If the nuclei are fixed at a distance R, the quantum state of the system is described by an angular wave function. The equation (1.20) is reduced to the equation of a *rigid rotator*

$$\left(\frac{\mathbf{J}^2}{2\mu R^2} - E_{rot}\right) Y_J^m(\theta, \phi) = 0. \tag{2.21}$$

This equation yields the following

$$\begin{aligned} \mathbf{J}^2 Y_J^m(\theta, \phi) &= J(J+1)\hbar^2 Y_J^m(\theta, \phi), & (2.22) \\ &= 2\mu R^2 E_{rot} Y_J^m(\theta, \phi). & (2.23) \end{aligned}$$

The rotational energies are then expressed by

$$\begin{aligned} E_{rot} &= \frac{\hbar^2}{2\mu R^2} J(J+1) & (2.24) \\ &= BJ(J+1), & (2.25) \end{aligned}$$

Table 2.6: Rotationless-vibrational energy levels of argonium $^{36}ArH^+$ in units of cm^{-1}.

v	$X\,^1\Sigma^+$	$A\,^1\Sigma^+$	$B\,^1\Pi$	$C\,^1\Sigma^+$	$D\,^1\Pi$
0	−32 424.701	−61.363	−187.036	−779.221	−739.390
1	−29 809.441	−13.703	−78.705	−462.728	−421.639
2	−27 313.744	−1.574	−23.275	−181.909	−145.584
3	−24 934.848		−3.791		
4	−22 669.965				
5	−20 516.329				
13	−7 014.710				
15	−4 647.520				
20	−790.945				
25	−13.112				
26	−2.637				

with

$$B = \frac{\hbar^2}{2\mu R^2}. \tag{2.26}$$

2.3.2 Results

With some adequate computational modifications, we adopted the AUTOMATIC LEVEL FINDER (ALF) subroutine, implemented in the LeRoy code LEVEL, fully described in [31]. This subroutine generates, in particular, the wave functions and bound energies of each (v, J) level needed in the computation of the requested transition matrix elements described by the equation (2.29).

We have calculated the rotationless-vibrational energy levels of ArH^+, which are listed in Table 2.6. The calculations showed that the $X\ ^1\Sigma^+$ potential holds up 27 vibrational levels, whereas the $A\ ^1\Sigma^+, B\ ^1\Pi$, $C\ ^1\Sigma^+$ and $D^1\Pi$ states can only accommodate a very limited number of vibrational levels: $3, 4, 3$, and 3, respectively.

2.3.3 Radiative lifetime

Among the best methods to assess the accuracy of our adopted potentials and dipole moments is the determination of the radiative lifetimes of the rotational-vibrational states. Radiative lifetime τ is the characteristic time that a molecule remains in its excited state before returning to the ground state by emitting a photon. It is defined by the inverse of the total spontaneous emission rate $\mathcal{A}\,(v'J'\Lambda')$ [35]

Table 2.7: Rotational-vibrational states relative to both argonium isotopes $^{36}ArH^+$ and $^{38}ArH^+$ in units of cm^{-1}.

v	J	$^{36}ArH^+$	$^{38}ArH^+$	Refs.	
0	0	−32 424.701	−32 425.663	31 101 ± 242	[32]
				32 066.48	[33]
0	5	−32 115.987	−32 117.386		
1	0	−29 809.441	−29 812.189	28 536 ± 242	[32]
				29 471.34	[33]
1	7	−29 255.304	−29 258.819		
2	8	−26 628.733	−26 634.027		
3	10	−23 930.705	−23 937.854		
5	20	−17 050.469	−17 062.994		

Table 2.8: Computed and measured rotational lines for $J = 1 - 0$ and $J = 2 - 0$ of $^{36}ArH^+$ and $^{38}ArH^+$ in MHz.

Transition	$^{36}ArH^+$	$^{38}ArH^+$	Refs.
$J = 1 \leftarrow 0$	617 704.99	616 828.47	
	617 525.226 ± 0.151	616 648.762 ± 0.083	[34]
	617 525.23 ± 0.15	616 648.76 ± 0.08	[4]
	617 525.149 ± 0.020	616 648.707 ± 0.020	[49]
$J = 2 \leftarrow 1$	1 234 969.74	1 233 217.96	
	1 234 602.75 ± 0.30	1 232 851.00 ± 0.04	[4]

$$\tau = \frac{1}{\mathcal{A}\left(v'J'\Lambda'\right)}. \tag{2.27}$$

We adopted the notation of simple prime ($\prime$) for the upper states and double prime ($\prime\prime$) for the lower states. Supposing the approximation on the angular momenta , $J = J' \simeq J''$, the total spontaneous emission rate corresponding to the transition from the upper bound levels $(v\prime J\Lambda')$ of the excited states to all the lower continuum $(\epsilon'' J\Lambda'')$ and bound levels $(v'' J\Lambda'')$ of the ground state $X^1\Sigma^+$ is calculated quantum-mechanically by the expression

$$\mathcal{A}\left(v'J\Lambda'\right) = \frac{32}{3}\left(\frac{\pi}{c}\right)^3 \frac{2-\delta_{0,\Lambda'+\Lambda''}}{2-\delta_{0,\Lambda'}} \times \left[\int_0^\infty \nu^3_{v'J\Lambda',\epsilon''J\Lambda''} M^2_{v'J\Lambda',\epsilon''J\Lambda''} d\epsilon'' + \sum_{v''} \nu^3_{v'J\Lambda',v''J\Lambda''} M^2_{v'J\Lambda',v''J\Lambda''}\right]. \tag{2.28}$$

where $M_{v'J\Lambda',\epsilon''J\Lambda''}$ represents the transition matrix elements defined as

$$M_{v'J\Lambda',\epsilon''J\Lambda''} = \int_0^\infty \psi'_{v'J\Lambda'}\left(R\right) D\left(R\right) \psi''_{\epsilon''J\Lambda''}\left(R\right) dR. \tag{2.29}$$

Table 2.9: Compilation of the lifetime values, in ns, computed for the rovibrational states.

	$C\,^1\Sigma^+$					$D\,^1\Pi$				
v	$J=0$	$J=1$	$J=2$	$J=3$	$J=4$	$J=0$	$J=1$	$J=2$	$J=3$	$J=4$
0	9.66	9.69	9.83	10.24	11.06	10.17	10.13	10.11	10.31	10.86
1	3.67	3.60	3.45	3.21	2.85	4.64	4.60	4.47	4.24	3.83
2	2.26	2.26	2.26	2.26	2.28	3.34	3.34	3.35	3.37	3.40

In this equation (2.28), the first term with the integral represents the probability of the spontaneous *bound-free* emission, while the second term with the sum represents the probability of the spontaneous *bound-bound* emission. Here, c denotes the velocity of light in vacuum and δ is the well known Kronecker symbol. Nonethless, the total spontaneous emission rate is expressed by

$$-\frac{dN}{N} = \mathcal{A}\,(v'J\Lambda')\,dt. \tag{2.30}$$

This relationship indicates that the number of molecules in the initial state $(v'J\Lambda')$ decreases exponentially over time

$$N = N_0 \exp(\frac{-t}{\tau}). \tag{2.31}$$

2.3.4 Results

The individual radiative lifetimes of the upper states involved in the transitions $X\,^1\Sigma^+ \leftarrow C\,^1\Sigma^+$ and $X\,^1\Sigma^+ \leftarrow D\,^1\Pi$ towards the deeper lower ground state $X\,^1\Sigma^+$ have been determined using the expressions (2.27) and (2.28) . Our results are listed in Table 2.9, such values might be a useful probe for assessing the accuracy of the ArH^+ potential sets. The *mean* lifetime $\overline{\tau}$ is computed with

$$\frac{1}{\overline{\tau}} = \frac{1}{3}\mathcal{A}_{X\leftarrow C}\,(v'_{\max}00) + \frac{2}{3}\mathcal{A}_{X\leftarrow D}\,(v'_{\max}01)\,. \tag{2.32}$$

According to the calculations, the highest rotationless vibrational states are both close to the dissociation limit. From Table 2.9, the present calculations lead to $\overline{\tau} \simeq 2.88\,\text{ns}$. Unfortunately, no published results were found in the literature to contrast with ours.

Chapter 3

Radiative association and charge transfer

The interpretation of radiative association (RA) and radiative charge transfer (RCT) processes may now be done using the potential energy curves and transition dipole moments that have been accurately constructed in the previous chapter (chapter 2).

3.1 Radiative association

Radiative association (RA) has been considered for the first time as one of the interstellar molecule formation mechanisms by Swings in 1942 [36, 37]. RA is currently described as a reactive process in which two smaller species, A and B, collide to form a larger molecule. The so-called *collision complex* AB^* is stabilized by spontaneous emission of radiation $h\nu$

$$A + B \longrightarrow AB^* \longrightarrow AB + h\nu. \tag{3.1}$$

This process is schematically illustrated in Fig. 3-1. RA is believed to play a crucial role in the synthesis of molecular species observed in diverse interstellar environments. In general, the formation of molecules through radiative association involves two main mechanisms: resonant and direct (non-resonant). The direct process occurs when the kinetic energy of the colliding particles is high enough to overcome any barrier (potential or centrifugal) present in the initial electronic state, and the spontaneous emission brings the system directly from the *continuum* to a *bound* level. On the other hand, the resonance contribution arises from quantum mechanical tunneling through the barrier, where the colliding particles form a *quasi-*

Figure 3-1: Schematic of radiative association process.

bound state. This thesis primarily concentrates on the direct radiative association and the main interest is to obtain the rate coefficients of RA.

The radiative association of the argon atoms Ar and hydrogen ions H^+ to form the ArH^+ ion occurs via one of the following processes:

1. ArH^+ formation in the ground state $X^1\Sigma^+$ via RA of $Ar(^1S)$ atom and H^+ ion, in *free-bound* transitions within the same electronic state $X^1\Sigma^+$, the process may be represented by

$$Ar(^1S) + H^+ \longrightarrow ArH^+\left(X^1\Sigma^+\right) \longrightarrow ArH^+\left(X^1\Sigma^+\right) + h\nu. \tag{3.2}$$

2. In transitions from *quasi-bound* levels of an excited electronic state $C^1\Sigma^+$ or $D^1\Pi$ to the *bound* levels of the ground electronic state $X^1\Sigma^+$, ArH^+ formation via RA of $Ar(^{1,3}P)$ atom and H^+ ion, may be represented by

$$Ar(^{1,3}P) + H^+ \longrightarrow ArH^+\left(C^1\Sigma^+\right) \longrightarrow ArH^+\left(X^1\Sigma^+\right) + h\nu \tag{3.3}$$

$$Ar(^{1,3}P) + H^+ \longrightarrow ArH^+\left(D^1\Pi\right) \longrightarrow ArH^+\left(X^1\Sigma^+\right) + h\nu. \tag{3.4}$$

These transitions occur into bound vibrational levels of the molecular states, and each of these reactions consists of two steps: the formation of the collision complex in the rotational quasi-bound levels and stabilization of the association by radiative association to bound rotation-vibration states by emitting a photon. The energy of the emitted photon for the radiative association into a bound vibrational state with vibrational

quantum number v'' and energy ϵ'' measured from the dissociation limit is given by

$$h\nu = \epsilon' - \epsilon'' + \mathcal{E}_{\rm tr}. \tag{3.5}$$

Here, ϵ' represents the initial energy of relative motion in the center of mass frame, ϵ'' represents the final energy, and $\mathcal{E}_{\rm tr}$ is the transition energy. The initial collision complex in the excited state, based on the potentials $C^1\Sigma^+$ and $D^1\Pi$ is stabilized via radiative electronic transition to bound levels of the ground state $X^1\Sigma^+$. We present our calculations of the rate coefficients for the reactions (3.2) and (3.3) using a fully quantum mechanical method. To do so, we require the cross section for radiative association, which depends on the possibilities to form and stabilize the association complex via radiative transition to a bound state.

3.1.1 Cross sections and rate coefficients

The calculation of the radiative association cross-section can be performed using different approaches, including classical or quantum dynamics. In this work, we applied the perturbation theory method to determine the RA cross-section. This approach is based on the dipole approximation for the interactions between the electric field and the molecular system. Under such approximations, the cross sections effective in radiative association can be obtained using the following expression

$$Q_{\rm a}(\epsilon') = \frac{64\pi^5}{3c^3k^2} \sum_{J'=0}^{J_{\rm max}} \sum_{v''=0}^{v_{\rm max}} \nu^3 \left[J' M^2_{v''J'\Lambda'';\epsilon'J'-1\Lambda'} + (J'+1) M^2_{v''J'\Lambda'';\epsilon'J'+1\Lambda'} \right], \tag{3.6}$$

where ϵ is the energy of the initial free state, Λ is the axial component of the electronic angular momentum, and v and J are the vibrational and rotational quantum numbers, respectively. c is the velocity of light and $k = \sqrt{2\mu\epsilon'^2/\hbar}$ denotes the wave number of the colliding species of reduced mass

$$\mu = \frac{M_{Ar} M_H}{(M_{Ar} + M_H - m_e)}. \tag{3.7}$$

In equation (3.6) , the transition matrix elements $M^2_{v''J'\Lambda'';\epsilon'J'\Lambda'}$ are taken between the higher *free* states ($\epsilon' J' \Lambda'$) and the lower *bound* states ($v'' J'' \Lambda''$).

To accurately determine the mean cross sections $\overline{Q}_{\rm a}(\epsilon')$ associated with RA, the statistical weight w of the involved molecular transitions is considered. The values of w are chosen as follows: $w = 1/2$ for the $X \leftarrow X$ transitions, $w = 1/6$ for the $X \leftarrow C$ transitions, and

$w = 2/6$ for the $X \leftarrow D$ transitions. Consequently, the mean cross sections can be computed using the formula

$$\overline{Q}_{\mathrm{a}}(\epsilon') = \frac{1}{2} Q_{\mathrm{a}}(X \leftarrow X) + \frac{1}{6} Q_{\mathrm{a}}(X \leftarrow C) + \frac{2}{6} Q_{\mathrm{a}}(X \leftarrow D). \tag{3.8}$$

After obtaining the cross-section for radiative association, it can be averaged over a Maxwellian velocity distribution to derive a temperature-dependent function known as the rate coefficient $\alpha(T)$. The calculation of the rate coefficient $\alpha(T)$ at temperature T can be performed using the following expression

$$\alpha_{\mathrm{a}}(T) = \left(\frac{8}{\pi\mu}\right)^{1/2} \left(\frac{1}{k_B T}\right)^{3/2} \int_0^\infty \overline{Q_{\mathrm{a}}}(\epsilon') \epsilon' \exp\left(-\frac{\epsilon'}{k_B T}\right) d\epsilon', \tag{3.9}$$

in this equation (3.9), k_B is the Boltzmann constant, μ denotes the reduced mass, and T represents the absolute temperature of the gas. The integral is performed over the Maxwellian velocity distribution. The statistically averaged value of the RA rate coefficients is determined by the relationship

$$\alpha_{\mathrm{a}}(T) = \frac{1}{3}\alpha_{X \leftarrow C}(T) + \frac{2}{3}\alpha_{X \leftarrow D}(T), \tag{3.10}$$

where here, $\alpha_{X \leftarrow C}(T)$ and $\alpha_{X \leftarrow D}(T)$ represent the rate coefficients for the transitions $X \leftarrow C$ and $X \leftarrow D$, respectively. The values of $1/3$ and $2/3$ are the statistical weights corresponding to the molecular transitions.

3.2 Radiative charge transfer

The *radiative charge transfer* (RCT) is a phenomenon observed when an ion collides with a neutral atom. When the ion approaches the atom closely enough, there is a possibility for the atom's valence electron to jump to the ion, resulting in the transfer of the ionic charge to the atom, accompanied by photon emission.

$$\mathrm{A} + \mathrm{B}^+ \longrightarrow \mathrm{A}^+ + \mathrm{B} + h\nu. \tag{3.11}$$

RCT process happens when electromagnetic radiation interacts with atoms, ions, or molecules. It is a crucial process in the fields of atomic and molecular physics, and it finds applications in plasma physics, astrophysics, and atmospheric science.

This process occurs, in particular, with the ionic ArH^+ system during the collisions from

the $A\,^1\Sigma^+$ and $B\,^1\Pi$ rotational *continuum* states to the rotational *continuum* of the ground state $X\,^1\Sigma^+$. The RCT process can be represented by the following reaction

$$\mathrm{Ar}\left(^1S\right) + \mathrm{H}^+ \longrightarrow \mathrm{Ar}^+\left(^2P\right) + \mathrm{H}\left(^2S\right) + h\nu. \tag{3.12}$$

The energy of the emitted photon $h\nu$ is determined by the expression

$$h\nu = \epsilon' - \epsilon'' + \mathcal{E}_{\mathrm{tr}}, \tag{3.13}$$

where ϵ' is the initial *free* energy of the relative motion of the colliding system, ϵ'' is its final *free* energy, and $\mathcal{E}_{\mathrm{tr}} = V'(\infty) - V''(\infty)$ is the transition energy. If k' and k'' are the *entrance* and *exit* wave numbers, respectively, defined as

$$\begin{cases} k' = \sqrt{2\mu\left[\epsilon' - V'(\infty)\right]} \\ \\ k'' = \sqrt{2\mu\left[\epsilon'' - V''(\infty) - h\nu\right]}. \end{cases} \tag{3.14}$$

3.2.1 Cross sections and rate coefficients

The *quantal* cross section for the present process (3.12) is given by [38, 39]

$$\frac{d}{d\epsilon''}Q_{\mathrm{c}}(\epsilon', \epsilon'') = \frac{8}{3}\left(\frac{\pi}{k'}\right)^2(\epsilon' - \epsilon'' + \mathcal{E}_{\mathrm{tr}})^3 \sum_{J'}\left[J' M^2_{J',J'-1} + (J'+1)M^2_{J',J'+1}\right], \tag{3.15}$$

where $M_{J',J''}$ represents the transition matrix elements defined as

$$M_{J',J''} = \int_0^\infty \psi'_{J'}(R)\, D(R)\, \psi''_{J''}(R)\, dR. \tag{3.16}$$

Here, $\psi'_{J'}(R)$ and $\psi''_{J''}(R)$ are the upper and lower *free* wave functions, respectively, J' is the *initial* rotational angular momentum quantum number, and $J'' = J' \pm 1$ is the *final* rotational quantum number.

The total cross section for radiative charge transfer $Q_{\mathrm{c}}(\epsilon')$ at energy ϵ' is obtained by integrating equation (3.15) over ϵ''

$$Q_{\mathrm{c}}(\epsilon') = \int_0^\infty \frac{d}{d\epsilon''}Q_{\mathrm{c}}(\epsilon', \epsilon'')\, d\epsilon''. \tag{3.17}$$

One should finally note that the total cross-sections $\overline{Q}_{\mathrm{c}}(\epsilon')$ effective in RCT are obtained as

the *mean* value computed by the statistically weighted sum

$$\overline{Q}_{\mathrm{c}}\left(\epsilon'\right) = \frac{1}{3} Q_{\mathrm{c}}\left(X \leftarrow A\right) + \frac{2}{3} Q_{\mathrm{c}}\left(X \leftarrow B\right). \tag{3.18}$$

The full quantum-mechanical description of the RCT mechanisms implies the computation of the temperature-dependent rate coefficients [40]

$$\alpha_{\mathrm{c}}\left(T\right) = \left(\frac{8}{\pi\mu}\right)^{1/2} \left(\frac{1}{k_B T}\right)^{3/2} \int_0^{\infty} \overline{Q}_{\mathrm{c}}\left(\epsilon'\right) \epsilon' \exp\left(-\frac{\epsilon'}{k_B T}\right) d\epsilon', \tag{3.19}$$

where k_B is the Boltzmann constant and T denotes the absolute temperature of the gas. This integral (3.19), performed over the Maxwellian velocity distribution, computes the *mean* of the energy-dependent RCT cross sections, $\overline{Q}_{\mathrm{c}}\left(\epsilon'\right)$. The statistically averaged value of the RCT rate coefficients is determined by the following relationship

$$\alpha_{\mathrm{c}}(T) = \frac{1}{3}\alpha_{X\leftarrow A}(T) + \frac{2}{3}\alpha_{X\leftarrow B}(T). \tag{3.20}$$

3.3 Results and discusions

Using the well-established PECs, PDM, and TDMs, we have performed quantum mechanical calculations to obtain the cross sections and rate coefficients for RA and RCT. The $X\,^1\Sigma^+ \leftarrow X\,^1\Sigma^+$ energy-dependent cross sections $Q_{\mathrm{a}}\left(\epsilon\right)$, which are effective in ArH^+ radiative association, have been calculated for two isotopologues, $^{36}ArH^+$ and $^{38}ArH^+$, and are presented in Fig. 3-2(a). The plots show that the resonance peaks match perfectly in position, particularly at higher energies, indicating that the isotopic effect is negligible. In addition, the computed cross sections $Q_{\mathrm{a}}\left(\epsilon\right)$, in connection with the transitions $X^1\Sigma^+ \leftarrow C^1\Sigma^+$ and $X^1\Sigma^+ \leftarrow D^1\Sigma^+$, are presented in Fig. 3-2(b). The $X^1\Sigma^+ \leftarrow C^1\Sigma^+$ transitions seem to be definitely the most probable and stronger than those due to the $X^1\Sigma^+ \leftarrow D^1\Sigma^+$ transitions. More precisely, the quasibound rovibrational levels of the initial states are primarily responsible for the observed resonance structures. However, due to the smallness of the ArH^+ reduced mass, only a very limited number of resonance peaks can be predicted, and these resonance peaks are strongly dependent on the constructed potentials [41].

Moreover, Fig. 3-3 illustrates the RCT cross sections $Q_{\mathrm{c}}\left(\epsilon\right)$ rising from the allowed transitions $X^1\Sigma^+ \leftarrow A^1\Pi$ and $X^1\Sigma^+ \leftarrow B^1\Pi$. The involved excited potential curves support extremely weak quasibound vibrational states, as seen in Table 2.6. This may explain the re-

duced number of resonance structures in the corresponding cross sections and the dominance of the $X^1\Sigma^+ \leftarrow A^1\Pi$ transitions compared to those of $X^1\Sigma^+ \leftarrow B^1\Pi$ [37]. At lower collision velocities, the ArH^+ system does not have enough kinetic energy to approach the potential barrier of the ground molecular state $X\,^1\Sigma^+$. But, above the energy 10^{-8} a.u., the system is able to penetrate the potential barrier and the regions where the $X\,^1\Sigma^+$ state contains a deep attractive well. In this region, there is essentially a sharp rise in the cross sections, and therefore numerous resonance lines appear, which are all caused by the rovibrational quasibound states of the ArH^+ molecule in the $X\,^1\Sigma^+$ electronic state.

Having now determined the quantal cross sections $Q_a(\epsilon)$ and $Q_c(\epsilon)$, it is hence possible to proceed with the computation of the temperature-dependent rate coefficients effective in radiative association and charge transfer, $\alpha_a(T)$ and $\alpha_c(T)$, respectively. With equation (3.19), the RA and RCT rates are computed in the temperature range of $10 - 10\,000$ K, and the numerical results are compiled in Tables 3.1 and 3.2. The former Table lists the generated $X^1\Sigma^+ \leftarrow X^1\Sigma^+$ data for both argon isotopes $^{36}ArH^+$ and $^{38}ArH^+$, whereas the latter table presents the RA and RCT results arising from the first and second excited transition sets.

The statistically averaged values of the rate coefficients can be further determined using the relationships (3.10) and (3.20). These values are presented in Table 3.2 as well. Firstly, we found a lack of published data regarding argonium's radiative association and charge transfer. Nevertheless, for the purpose of comparison, Kraemer *et al* [37] published their graphical results of the rate coefficients $\alpha_a(T)$ for the formation of the ionic dimer ArH^+ in the ground state $X\,^1\Sigma$. Our graphical estimation from Fig. 9 of Ref. [37] yields the values $\alpha_a(10) \simeq 5.6 \times 10^{-19}$, $\alpha_a(100) \simeq 3.8 \times 10^{-19}$, and $\alpha_a(1000) \simeq 2.3 \times 10^{-19}\,cm^3\,s^{-1}$ for three particular temperatures. Although the estimated RA rate coefficients are not in this case exactly the same, the discrepancies are important, but the magnitudes are quite similar.

On the other hand, due to the lack of published RCT data on ArH^+, we had to compare our results with those obtained from collisions among species belonging to families close to Ar/Ar^+ and H^+/H. Indeed, the RCT rates at $T = 300$ K in connection with interactions of Ar with He^+ and Ne with He^+ yielded the values $\alpha_c(300) \simeq 9.86 \times 10^{-15}$ in Babb and McLaughlin [42] and $\alpha_c(300) \simeq 5 \times 10^{-16}\,cm^3\,s^{-1}$ in Liu *et al.* [43], respectively. Our generated weighted value at the same temperature is equal to $\alpha_c(300) \simeq 5.785 \times 10^{-18}\,cm^3\,s^{-1}$.

The graphical representations of the *average* RA and RCT rate coefficients are illustrated in Fig. 3-4. The upper Fig. 3-4 (a) represents the statistically weighted average results of the ArH^+ RA rate coefficients, depending on the considered isotopes. The lower Fig. 3-4

(b) displays the profiles of the average rate coefficients $\alpha_{\mathrm{a}}(T)$ and $\alpha_{\mathrm{c}}(T)$ obtained in terms of temperature. The plots demonstrate that, in the same gaseous environment, the RCT phenomena dominate the RA. The particular investigation on the $\mathrm{Ne} - \mathrm{He}^{+}$ collisions conducted by Liu *et al* [43] concluded that the RA and RCT rate coefficients, in the temperature range $10 - 10\,000\,\mathrm{K}$, are of the same magnitude. However, the present calculations prove the predominance of the RCT processes over the RA ones.

Finally, the *average* RA rate coefficient has been fitted with the polynomial expression

$$\alpha_{\mathrm{a}}(T) = \sum_{j=0}^{9} a_j T^j. \tag{3.21}$$

It turns out that the best fits can be obtained with the first *ten* monomials. Table 3.4 gathers these monomials. Whereas, the average RCT rate coefficient has been fitted with the expression

$$\alpha_{\mathrm{c}}(T) = a \left(\frac{T}{1000} \right)^{b} \tag{3.22}$$

with a and b being two constants ($a = 9.620 \times 10^{-18}$, $b = 0.287$). For $100 \leqslant T \leqslant 10\,000\,\mathrm{K}$, the present fitting results are plotted in Figs. 3-5 and 3-6. At higher temperatures, the concordances are specifically better.

Table 3.1: $X - X$ RA rate coefficients (in $\mathrm{cm^3\,s^{-1}}$) computed at some temperatures T (in K). The notation $a[-n]$ stands for $a \times 10^{-n}$.

Temperature	$X \leftarrow X$	
T (K)	$^{36}ArH^+$	$^{38}ArH^+$
10	1.173[−19]	1.012[−19]
50	9.899[−20]	1.018[−19]
100	9.825[−20]	9.631[−20]
200	9.949[−20]	9.221[−20]
300	9.712[−20]	9.027[−20]
400	9.397[−20]	8.833[−20]
500	9.087[−20]	8.619[−20]
600	8.802[−20]	8.398[−20]
700	8.543[−20]	8.179[−20]
800	8.309[−20]	7.969[−20]
900	8.099[−20]	7.769[−20]
1000	7.909[−20]	7.582[−20]
2000	6.810[−20]	6.326[−20]
3000	6.581[−20]	5.814[−20]
4000	6.814[−20]	5.715[−20]
5000	7.263[−20]	5.828[−20]
6000	7.757[−20]	6.019[−20]
7000	8.198[−20]	6.205[−20]
8000	8.542[−20]	6.350[−20]
9000	8.781[−20]	6.442[−20]
10000	8.920[−20]	6.480[−20]

Table 3.2: RA rate coefficients (in $\mathrm{cm^3\,s^{-1}}$) computed at some temperatures T (in K). The notation $a[-n]$ stands for $a \times 10^{-n}$.

Temperature	RA rate coefficients		
T (K)	$C \to X$	$D \to X$	Average
10	4.271[−19]	4.548[−21]	1.454[−19]
50	4.019[−19]	7.883[−21]	1.392[−19]
100	3.823[−19]	9.794[−21]	1.339[−19]
200	3.686[−19]	1.246[−20]	1.312[−19]
300	3.712[−19]	1.481[−20]	1.336[−19]
400	3.805[−19]	1.693[−20]	1.381[−19]
500	3.923[−19]	1.883[−20]	1.433[−19]
600	4.051[−19]	2.053[−20]	1.487[−19]
700	4.180[−19]	2.205[−20]	1.540[−19]
800	4.306[−19]	2.345[−20]	1.592[−19]
900	4.430[−19]	2.473[−20]	1.641[−19]
1000	4.548[−19]	2.591[−20]	1.689[−19]
2000	5.390[−19]	3.332[−20]	2.019[−19]
3000	5.718[−19]	3.547[−20]	2.142[−19]
4000	5.832[−19]	3.558[−20]	2.181[−19]
5000	5.875[−19]	3.511[−20]	2.192[−19]
6000	5.883[−19]	3.449[−20]	2.191[−19]
7000	5.860[−19]	3.380[−20]	2.178[−19]
8000	5.806[−19]	3.304[−20]	2.156[−19]
9000	5.724[−19]	3.223[−20]	2.123[−19]
10000	5.619[−19]	3.137[−20]	2.082[−19]

Table 3.3: RCT rate coefficients (in $\mathrm{cm^3\,s^{-1}}$) computed at some temperatures T (in K). The notation $a[-n]$ stands for $a \times 10^{-n}$.

Temperature	RCT rate coefficients		
T (K)	$A \to X$	$B \to X$	Average
10	1.420[−18]	1.142[−20]	4.811[−19]
50	3.466[−18]	1.957[−20]	1.168[−18]
100	7.611[−18]	2.751[−20]	2.555[−18]
200	1.326[−17]	4.569[−20]	4.452[−18]
300	1.723[−17]	6.113[−20]	5.785[−18]
400	2.029[−17]	7.329[−20]	6.812[−18]
500	2.271[−17]	8.297[−20]	7.626[−18]
600	2.468[−17]	9.084[−20]	8.286[−18]
700	2.631[−17]	9.737[−20]	8.836[−18]
800	2.770[−17]	1.029[−19]	9.302[−18]
900	2.890[−17]	1.076[−19]	9.705[−18]
1000	2.995[−17]	1.117[−19]	1.006[−17]
2000	3.636[−17]	1.368[−19]	1.221[−17]
3000	3.996[−17]	1.516[−19]	1.342[−17]
4000	4.271[−17]	1.638[−19]	1.434[−17]
5000	4.511[−17]	1.752[−19]	1.515[−17]
6000	4.736[−17]	1.866[−19]	1.591[−17]
7000	4.954[−17]	1.980[−19]	1.664[−17]
8000	5.170[−17]	2.097[−19]	1.737[−17]
9000	5.386[−17]	2.217[−19]	1.810[−17]
10000	5.604[−17]	2.341[−19]	1.884[−17]

Table 3.4: Fitting's constants of the average RA rate coefficients.

j	a_j
0	+5.051[−19]
1	+2.265[−20]
2	−2.261[−23]
3	+1.359[−26]
4	−4.968[−30]
5	+1.134[−33]
6	−1.621[−37]
7	+1.408[−41]
8	−6.787[−46]
9	+1.392[−50]

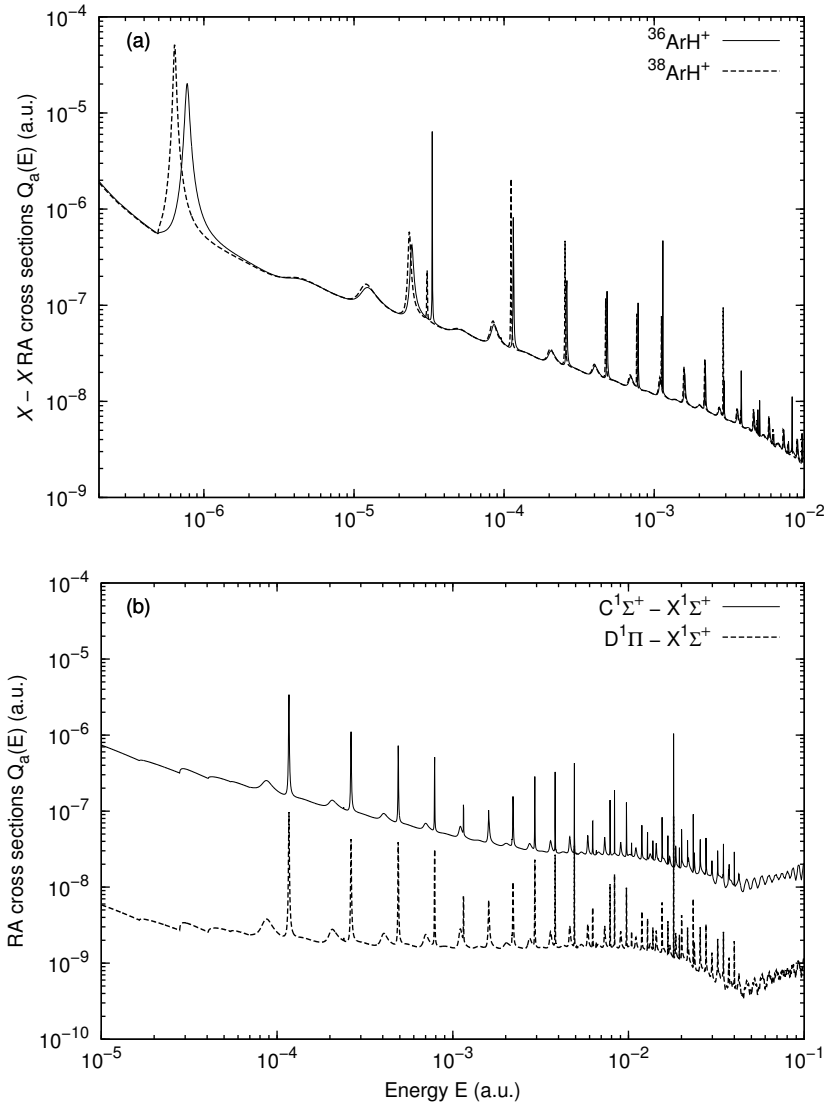

Figure 3-2: ArH^+ radiative association cross sections in terms of energy in connection with the (a) $X \leftarrow X$ transitions for both isotopes $^{36}ArH^+$ and $^{36}ArH^+$, and with the (b) $X \leftarrow C$ and $X \leftarrow D$ $^{36}ArH^+$ transitions.

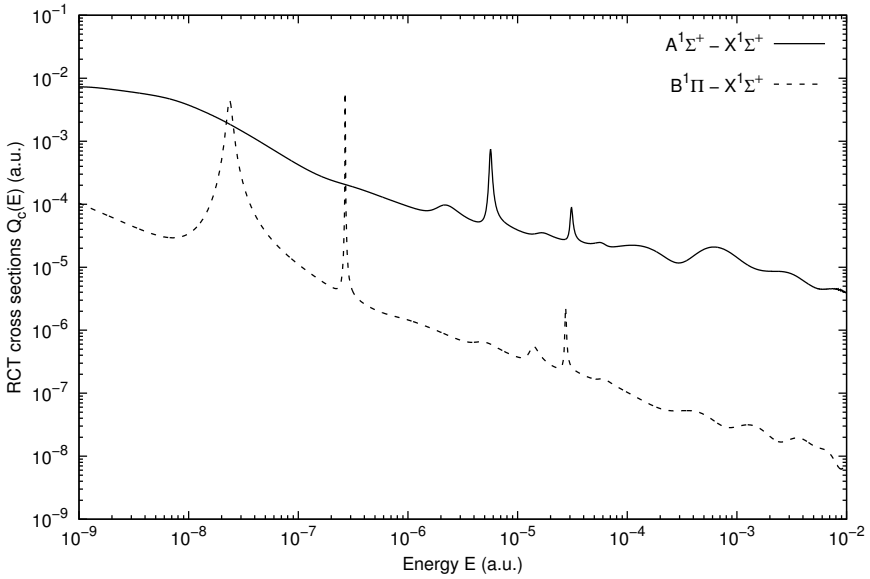

Figure 3-3: $^{36}ArH^+$ radiative charge transfer cross sections in terms of energy in connection with the $X \leftarrow A$ and $X \leftarrow B$ transitions.

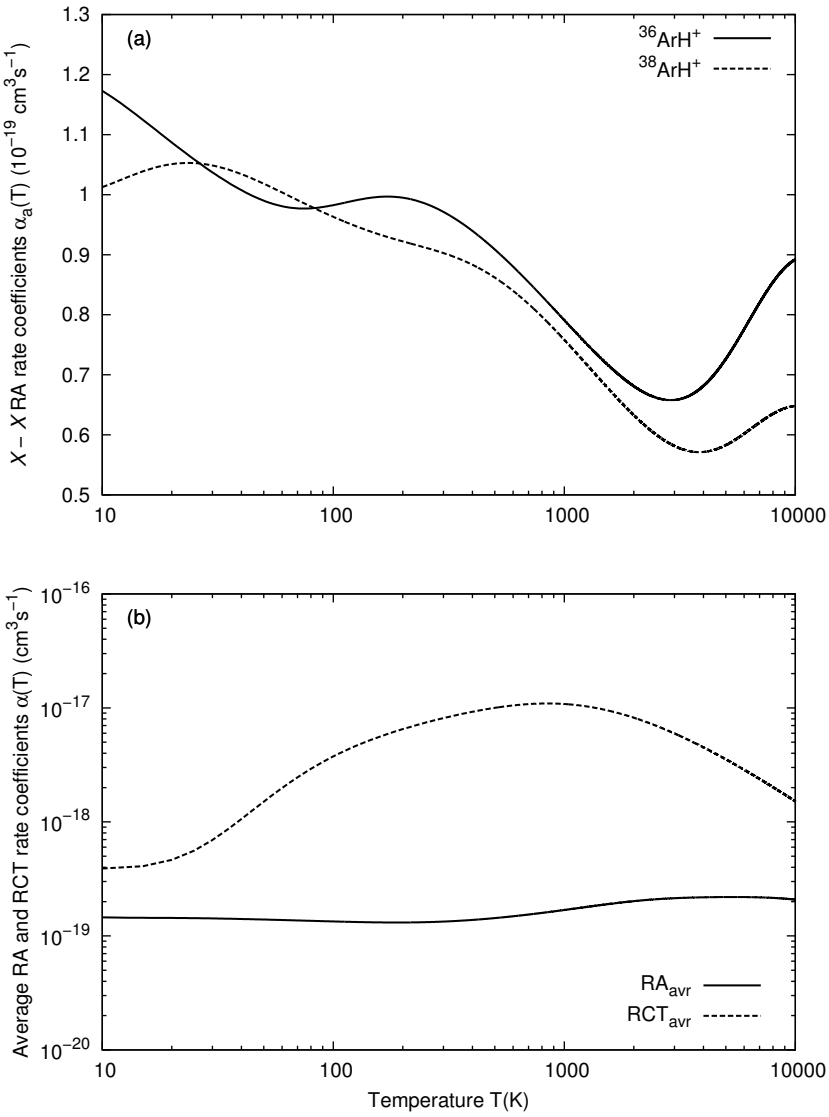

Figure 3-4: The variation of RA and RCT rate coefficients with temperature. The upper figure (a) displays the isotopic effects on the $X-X$ rate, whereas the lower figure (b) compares the average RA and RCT rates.

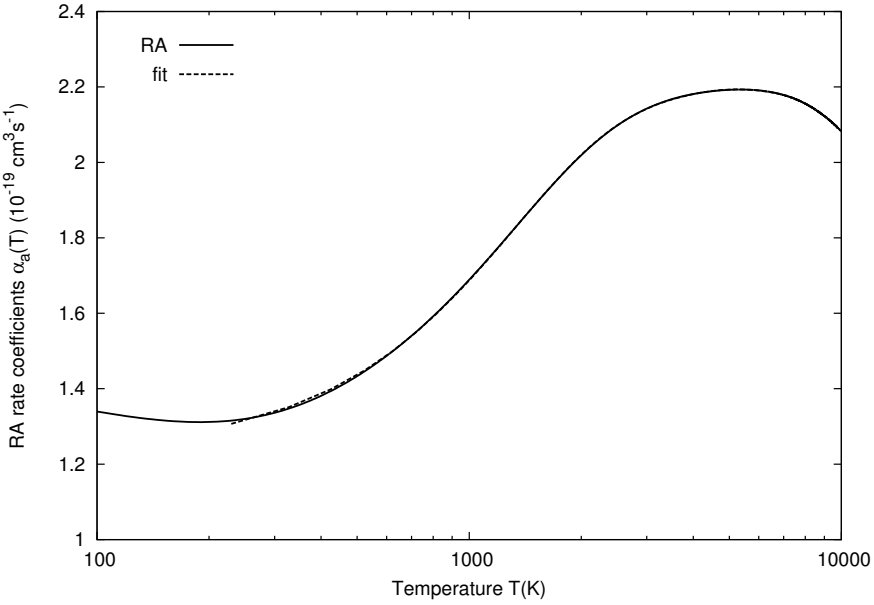

Figure 3-5: Fitting of the average RA rate coefficients to the polynomial expression given in equation 3.21.

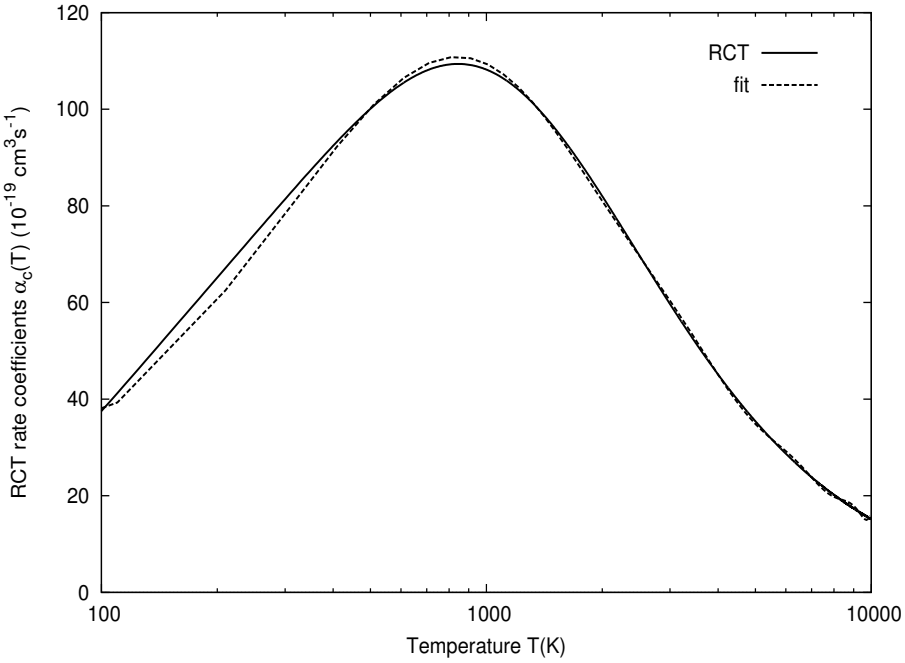

Figure 3-6: Fitting of the average RCT rate coefficients to the polynomial expression given in 3.21.

Chapter 4

Conclusion and outlook

This thesis presents an extensive characterization of the argonium molecular species ArH^+, which was detected in the extragalactic Crab nebula. The formation of this molecule in such a harsh environment was unexpected. The main purpose of this work is to examine radiative association (RA) and radiative charge transfer (RCT), which are two processes that might be responsible for the formation of argonium. To accomplish this task, we started by constructing the potential energy curves (PECs) in the singlet states, as well as their corresponding permanent dipole moments (PDM) and transition dipole moments (TDMs). This construction is carried out smoothly and appropriately in three regions of separation from the adopted *ab-initio* data and the appropriate analytical forms. To evaluate the accuracy of these PECs, PDMs, and TDMs, we computed several physical parameters, including the spectroscopic parameters, ro-vibrational levels, and radiative lifetimes. Our results are typically consistent with other published values, which have given us confidence in the validity of our present constructions. Then, using our constructed potentials, we have determined the wave functions of the free and bound states by solving numerically the radial wave equation. Over a wide range of energy and temperature, we calculated quantum mechanically the cross sections and rate coefficients for the formation of ArH^+ via the radiative association and radiative charge transfer. Our results have shown predominance of RCT over RA.

Appendix A

Physical constants and units

In atomic units, $\hbar = e = E_h = 1$.

Table A.1: Relative atomic masses of argon's isotopologues and hydrogen atom.

Atom	Atomic Masses (u)	Refs
^{36}Ar	35.967545106(29)	[13]
^{38}Ar	37.9627324(4)	[13]
^{40}Ar	39.9623831225(29)	[13]
^{1}H	1.00782503207(10)	[13]

Table A.2: List of fundamental physical constants used in this thesis.

Physical constant	Symbol	Value	Unit
Speed of light in vacuum	c	299792458	m s^{-1}
Planck constant	h	$6.62607015 \times 10^{-34}$	J s
Reduced Planck constant	$\hbar = \frac{h}{2\pi}$	$1.054571817 \times 10^{-34}$	J s
Boltzmann constant	k_B	1.380649×10^{-23}	$\mathrm{J\,K^{-1}}$
Elementary charge	e	$1.602176634 \times 10^{-19}$	C
Electron rest mass	m_e	$9.1093837015(28) \times 10^{-31}$	kg
Bohr radius	a_0	$5.29177210903(80) \times 10^{-11}$	m

Table A.3: List of atomic units.

Physical quantity	Symbol	Value	Unit
Length	a_0	$5.29177210903(80) \times 10^{-11}$	m
Energy	E_h	$4.3597447222071(85) \times 10^{-18}$	J
Mass	m_e	$9.1093837015(28) \times 10^{-31}$	kg
Electric potential	$\frac{E_h}{e}$	27.211386245988(53)	V
Electric dipole moment	ea_0	$8.4783536255(13) \times 10^{-30}$	C m

Table A.4: List of energy equivalents.

	J	$\mathrm{cm^{-1}}$	K	eV
J	1	$5.03411657 \times 10^{24}$	7.242971×10^{22}	$6.241509074 \times 10^{18}$
$\mathrm{cm^{-1}}$	$1.98644585 \times 10^{-23}$	1	1.438777	$1.23884198 \times 10^{-4}$
K	7.242971×10^{22}	0.6950348	1	8.617333×10^{-5}
eV	$1.602176634 \times 10^{-19}$	8.06554394×10^{3}	1.604518×10^{4}	1

Appendix B

Transition rates for absorption and emission of radiation

The absorption and emission of radiation are described by the Hamiltonian

$$\hat{H} = \hat{H}_0 + \hat{V}(t), \tag{B.1}$$

where $\hat{H}_0$ represents the time-independent component, and $\hat{V}$ represents the time-dependent component

$$\hat{V}(t) = \hat{\nu} e^{i\omega t} + \hat{\nu}^{\dagger} e^{-i\omega t} \tag{B.2}$$

with $\hat{\nu}$ is a time-independent operator, ω is the transition frequency. The transition probability corresponding to a transition from an initial state $|\psi_i\rangle$ of energy E_i to another state $\langle\psi_f|$ of energy E_f is given by [64]

$$P_{if}(t) = \frac{2\pi t}{\hbar} \left|\langle\psi_f|\hat{V}|\psi_i\rangle\right|^2 \delta(E_f - E_i) \tag{B.3}$$

The transition rate, which is defined as a transition probability per unit time is given by

$$\Gamma_{if} = \frac{2\pi}{\hbar} \left|\langle\psi_f|\hat{V}|\psi_i\rangle\right|^2 \delta(E_f - E_i) \tag{B.4}$$

In the case of photon emission, where the photon has energy $\hbar\omega_k$, wave number $\vec{k}$, wave number λ, and polarization ε, the system undergoes a transition from an initial sate $|\Phi_i\rangle = |\psi_i\rangle|n_{\lambda,\vec{k}}\rangle$ to the final state $|\Phi_f\rangle = |\psi_f\rangle|n_{\lambda,\vec{k}} + 1\rangle$. This can be achieved formally by creating

a photon, i.e., by applying the creation operator $\hat{a}^{\dagger}_{\lambda,\vec{k}}$ on $|n_{\lambda,\vec{k}}\rangle$

$$\langle\Phi_f|\hat{v}^{\dagger}_{\lambda,\vec{k}}|\Phi_i\rangle = \frac{e}{m_e}\sqrt{\frac{2\pi\hbar}{\omega_k V}}\langle\psi_f|e^{-i\vec{k}\vec{r}}\vec{\varepsilon}^{*}_{\lambda}.\vec{P}|\psi_i\rangle\langle n_{\lambda,\vec{k}}+1|\hat{a}^{\dagger}_{\lambda,\vec{k}}|n_{\lambda,\vec{k}}\rangle \tag{B.5}$$

$$= \frac{e}{m_e}\sqrt{\frac{2\pi\hbar}{\omega_k V}}\sqrt{n_{\lambda,\vec{k}}+1}\langle\psi_f|e^{-i\vec{k}\vec{r}}\vec{\varepsilon}^{*}_{\lambda}\vec{P}|\psi_i\rangle. \tag{B.6}$$

In the case of photon absorption, the system undergoes a transition from an initial state $|\Phi_i\rangle = |\psi_i\rangle|n_{\lambda,\vec{k}}\rangle$ to the final state $|\Phi_f\rangle = |\psi_f\rangle|n_{\lambda,\vec{k}}-1\rangle$. This can be achieved formally by applying the annihilation operator $\hat{a}_{\lambda,\vec{k}}$ on $|n_{\lambda,\vec{k}}\rangle$

$$\langle\Phi_f|\hat{v}_{\lambda,\vec{k}}|\Phi_i\rangle = \frac{e}{m_e}\sqrt{\frac{2\pi\hbar}{\omega_k V}}\langle\psi_f|e^{i\vec{k}\vec{r}}\vec{\varepsilon}_{\lambda}.\vec{P}|\psi_i\rangle\langle n_{\lambda,\vec{k}}-1|\hat{a}_{\lambda,\vec{k}}|n_{\lambda,\vec{k}}\rangle \tag{B.7}$$

$$= \frac{e}{m_e}\sqrt{\frac{2\pi\hbar}{\omega_k V}}\sqrt{n_{\lambda,\vec{k}}}\langle\psi_f|e^{-i\vec{k}\vec{r}}\vec{\varepsilon}_{\lambda}\vec{P}|\psi_i\rangle \tag{B.8}$$

where $\hat{v}^{\dagger}_{\lambda,\vec{k}}$ and $\hat{v}_{\lambda,\vec{k}}$ are given by

$$\hat{v}^{\dagger}_{\lambda,\vec{k}} = \frac{e}{m_e}\sqrt{\frac{2\pi\hbar}{\omega_k V}}\hat{a}^{\dagger}_{\lambda,\vec{k}}e^{-i\vec{k}\vec{r}}\vec{\varepsilon}^{*}_{\lambda}.\vec{P} \tag{B.9}$$

$$\hat{v}_{\lambda,\vec{k}} = \frac{e}{m_e}\sqrt{\frac{2\pi\hbar}{\omega_k V}}\hat{a}_{\lambda,\vec{k}}e^{i\vec{k}\vec{r}}\vec{\varepsilon}_{\lambda}.\vec{P} \tag{B.10}$$

The transition rates corresponding to the emission or absorption of a photon can be obtained as follows

$$\Gamma^{emi}_{i\to f} = \frac{4\pi^2e^2}{m_e^2\omega_k V}(n_{\lambda,\vec{k}}+1)\left|\langle\psi_f|e^{-i\vec{k}\vec{r}}\vec{\varepsilon}^{*}_{\lambda}.\vec{P}|\psi_i\rangle\right|^2\delta(E_f-E_i+\hbar\omega_k), \tag{B.11}$$

$$\Gamma^{abs}_{i\to f} = \frac{4\pi^2e^2}{m_e^2\omega_k V}n_{\lambda,\vec{k}}\left|\langle\psi_f|e^{i\vec{k}\vec{r}}\vec{\varepsilon}_{\lambda}.\vec{P}|\psi_i\rangle\right|^2\delta(E_f-E_i+\hbar\omega_k). \tag{B.12}$$

Appendix C

Article and communications

The work presented in this thesis was the subject of an article in *Journal of Physics B: Atomic, Molecular and Optical Physics,* as well as six international communications and two national communications.

C.1 Article

F. Talhi and M. Bouledroua, *The phenomena of radiative association and charge transfer observed in* $Ar^+ + H$ *and* $Ar + H^+$ *collisions,* Journal of Physics B: Atomic, Molecular and Optical Physics **56,** 015201 (2023).

C.2 Communications

- **M. Bouledroua, F. Talhi**, *Radiative association of* ^{36}Ar *and* ^{38}Ar *with ionic hydrogen,* 21st International Mass Spectrometry Conference (IMSC2016), University of Ottawa, 20-26 August 2016, Toronto, Canada.
- **F. Talhi, M. Bouledroua**, *Radiative association of* ^{36}Ar *and* ^{38}Ar *with ionic hydrogen,* The Fourth Algerian Conference in Astronomy and Astrophysics (ACAA17), University of Khenchla, 25-29 Mars 2017, Khenchla, Algeria.
- **F. Talhi, M. Bouledroua**, *Radiative association of* ^{36}Ar *and* ^{38}Ar *with ionic hydrogen,* 6th Olympiad of Theoratical Physics (OPT), University of Batna, 17-18 April 2017, Batna, Algeria.

- **M. Bouledroua, F. Talhi**, *Radiative association of* $^{36}Ar^+$ *and* $^{38}Ar^+$ *with hydrogen,* Workshop on Astrophysical Opacities, Western Michigan University, 01-04 August 2017, Kalamazoo, Michigan, USA.

- **F. Talhi, M. Bouledroua,** *Radiative association of* ^{36}Ar *and* ^{38}Ar *with ionic hydrogen,* 1st International Conference on Radiations and Applications (ICRA 17), Houari Boumediene University of Science and Technology (USTHB), 20-23 November 2017, Algiers, Algeria.

- **M. Bouledroua, F. Talhi,** *Radiative charge transfer and association in* $Ar + H^+$ *and* $Ar^+ + H$ *collisions,* Astrophemistry 2018: Past, Present, & Future, California Institute of Technology, 10-14 July 2018, Pasadena, California, USA.

- **F. Talhi, M. Bouledroua,** *Radiative association of* ^{36}Ar *and* ^{38}Ar *with ionic hydrogen,* Première conference internationale sur les collisions de particules chargées avec des cibles atomiques et moléculaires (CPCAM1), University of Setif1, 23-25 Septembre 2018, Setif, Algeria.

- **F. Talhi, M. Bouledroua,** *The first noble gas molecular ion detected in space* ArH^+, The Third Arab Winter School for Astrophysics (Ar AS SfA-3), American University of Beirut, 12-17 November 2018, Beirut, Lebanon,.

Bibliography

[1] M.J. Barlow, B.M. Swinyard, P.J. Owen, J. Cernicharo, H.L. Gomez, R.J. Ivison, O. Krause, T.L. Lim, M. Matsuura, S. Miller, G. Olofsson, and E.T. Polehampton, Science **342,** 1343 (2013).

[2] H.S.P. Müller, Endres, C.P., Stutzki, J., & Schlemmer, S.2013, in AIP Conf. Ser., Vol.1545 (New York: AIP), **96.**

[3] P. Schilke, D.A. Neufeld, H.S.P. Müller, C. Comito, E.A. Bergin, D.C. Lis, M. Gerin, J.H. Black, M. Wolfire, N. Indriolo, J.C. Pearson, K.M. Menten, B. Winkel, Á. Sánchez-Monge, T. Möller, B. Godard, and E. Falgarone, Astron. Astrophys. **566,** A29 (2014).

[4] H.S.P. Müller, S. Muller, P. Schilke, E.A. Bergin, J.H. Black, M. Gerin, D.C. Lis, D.A. Neufeld, and S. Suri, Astron. Astrophys. **582,** L4 (2015).

[5] D.A. Neufeld, M. Goto, T.R. Geballe, R. Güsten, K.M. Menten, and H. Wiesemeyer, Astrophys. J. **894,** 37 (2020).

[6] F.D. Priestley, M.J. Barlow, and S. Viti, Mon. Not. R Astron. Soc. **472,** 4444 (2017).

[7] G. C Maitland, M. Rigby, E. B. Smith, and W. A. Wakeham. *Intermolecular Forces: Their Origin and Determination.* Clarendon Press, Oxford, (1981).

[8] B.H.Bransden and M.R.C. Mcdowell, *Charge Exchange and the Theory of Ion-Atom Collisions, (*Clerendon Press, Oxford, 1992).

[9] G. Herzberg. *Molecular Spectra and Molecular Structure, Volume I, Spectra of Diatomic Molecules.* Krieger Publishing Company, Malabar, 2nd edition, 1989.

[10] J. M. Brown and A. Carrington. *Rotational Spectroscopy of Diatomic Molecules.* Cambridge University Press, Cambridge, 2003.

[11] W.H. Press, B.P.Flannery, S.A. Teukolsky, and W.T. Vetterling, *Numerical Recipes. The Art of Scientific Computing*, (Cambridge University Press, New York, 1987).

[12] A.A. Radzig and B.M. Smirnov, References Data on Atoms, Molecules, and Ions, (Springer-Verlag, Berlin, 1985).

[13] NIST Chemistry Webook, NIST Standard Reference Database Number 69, National Institute of Standards and Technology, Gaithersburg MD, 20899.

[14] P. Schwerdtfeger and J.K. Nagle, Mol. Phys. **117,** 1200 (2018).

[15] M. Miller and B. Bederson, Adv. At. Mol. Phys. **13,** 1 (1977).

[16] T.N. Olney, N.M. Cann, G. Cooper, and C.E. Brion, Chem. Phys. **223,** 59 (1997).

[17] K.T. Tang, J.M. Norbeck, and P.R. Certain, J. Chem. Phys. **64,** 3063 (1976).

[18] J. Mitroy and J.-Y. Zhang, Phys. Rev. A **76,** 032706 (2007).

[19] G. Figari, G.F. Musso, and V. Magnasco, Mol. Phys. **50,** 1173 (1983).

[20] A.J. Thakkar, H. Hettema, and P.E.S. Wormer, J. Chem. Phys. **97,** 3252 (1992).

[21] D. Spelsberg and W. Meyer, J. Phys. Chem. **100,** 14637 (1996).

[22] A.V. Stolyarov and M.S. Child, Phys. Chem. Chem. Phys. **7,** 2259 (2005).

[23] A.B. Alekseyev, H.-P. Liebermann, and R.J. Buenker, Phys. Chem. Chem. Phys. **9,** 5088 (2007).

[24] P. Rosmus, Theoret. Chim. Acta **51,** 359 (1979).

[25] H. Hotop, T.E. Roth, M.-W. Ruf, A.J. Yencha, Theor. Chem. Acc. **100,** 36 (1998).

[26] M.A. Maltsev I.V. Morozov, and E.L. Osina, High Temp. **57,** 335 (2019).

[27] X. Chu and A. Dalgarno, Phys. Rev. A **66,** 024701 (2002).

[28] U. Volz and H. Schmoranzer, Phys. Scr. T **65,** 48 (1996)**.**

[29] C.Cohen-Tanoudji, F. Laloë, and B. Diu, *Mécanique Quantique*, Tomes I et II (Hermann, Paris, 1973).

[30] G. Herzberg, *Molecular Spectra and Molecular Structure*, Vol.I : Spectra of Diatomic Molecules, (D. van Nostrand Co., Princeton, 1963).

[31] Journal of Quantitative Spectroscopy and Radiative Transfer. **186**, 167 (2017).

[32] J. Lorenzen, H. Hotop, M.W. Ruf, and H. Morgner, Z. Physik. A **297,** 19 (1980).

[33] D.M. Hirst, M.F. Guest, and A.P. Rendell, Mol. Phys. **77,** 279 (1992).

[34] M. Cueto, J. Cernicharo, M.J. Barlow, B.M. Swinyard, V.J. Herrero, I. Tanarro, and J.L. Doménech, Astrophys. J. Lett. **783,** L5 (2014).

[35] B.H. Bransden and C.J. Joachim, *Physics of Atoms and Molecules*, (Longman, New York, 1986).

[36] P. Swings, Astrophys.J.**95,** 270-280 (1942)

[37] W.P. Kraemer, M. Juřek, and V. Špirko, *Quantum-mechanical studies of radiative association reactions: formation of* HeH^+, NeH^+ *and* ArH^+ in Advanced Series in Physical Chemistry, 516–553 (1997).

[38] L.B. Zhao, P.C. Stancil, J.P. Gu, H.-P. Liebermann, Y. Li, P. Funke, R.J. Buenker, B. Zygelman, M. Kimura, and A. Dalgarno, Astrophys. J **615,** 1063 (2004).

[39] X. Lin, Y. Peng, Y. Wu, J. Wang, R. Janev, and B. Shao, Astron. Astrophys. **598,** A75 (2017).

[40] S.V. Antipov, M. Gustafsson, and G. Nyman, Mon. Not. Roy. Astron. Soc. **430,** 946 (2013).

[41] H. da Silva Jr, M. Raoult, M. Aymar, and O. Dulieu, New J. Phys. **17,** 045015 (2015).

[42] J. Babb and B.M. McLaughlin, Astro. Phys. J. **860,** 151 (2018).

[43] X.J. Liu, Y.Z. Qu, B.J. Xiao, C.H. Liu, Y. Zhou, J.G. Wang, and R.J. Buenker, Phys. Rev. A **81,** 022717 (2010).

[44] R. Güsten, H. Wiesemeyer, D. Neufeld, K.M. Menten, U.U. Graf, K. Jacobs, B. Klein, O. Ricken, C. Risacher, and J. Stutzki, Nature **568,** 357 (2019).

[45] H.S.P. Müller, F. Schlöder, S. Thorwirth, G. Winnewisser, The Cologne Database for Molecular Spectroscopy, CDMS. In: S. Pfalzner, C. Kramer, C. Straubmeier, and A. Heithausen (Eds) The Dense Interstellar Medium in Galaxies. Springer Proceedings in Physics, vol 91. (Springer, Berlin, Heidelberg , 1997).

[46] J.R. Hamilton, A. Faure, and J. Tennyson, Mon. Not. R. Astron. Soc. **455,** 3281 (2016).

[47] E. Roueff, A.B. Alekseyev, and J. Le Bourlot, Astron. Astrophys. **566,** A30 (2014).

[48] J.A. Coxon and P.G. Hajigeorgiou, J. Mol. Spectrosc. **330,** 63 (2016).

[49] L. Bizzocchi, L. Dore, C.D. Esposti, and F. Tamassia, Astrophys. J. Lett. **820,** L26 (2016).

[50] A. Abdoulanziz, F. Colboc, D.A. Little, Y. Moulane, J. Zs Mezei, E. Roueff, J. Tennyson, I.F. Schneider, and V. Laporta, Mon. Not. R. Astron. Soc. **479,** 2415 (2018).

[51] P.J. Dagdigian, Mon. Not. R. Astron. Soc. **477,** 802 (2018).

[52] B. Bastian, E. Carrascosa, A. Kaiser, J. Meyer, T. Michaelsen, G. Czakób, W.L. Hase, and R. Wester, Int. J. Mass Spectrom. **438,** 175 (2019).

[53] F.A. Gianturco and P. Gori Giorgi, Astrophys. J. **479,** 560 (1997).

[54] R.C. Forrey, J.F. Babb, E.D.S. Courtney, R.T. McArdle, and P.C. Stancil, Astrophys. J **898,** 86 (2020).

[55] C.J.H. Schutte, Chem. Phys. Lett. **345,** 525 (2001).

[56] C.J.H. Schutte, Chem. Phys. Lett. **350,** 181 (2001).

[57] C.J.H. Schutte, Chem. Phys. Lett. **353,** 389 (2002).

[58] J.A. Coxon and M. Molski, J. Mol. Spectrosc. **223,** 51 (2004).

[59] A. Kirrander, M.S. Child, and A.V. Stolyarov, Phys. Chem. Chem. Phys. **8,** 247 (2006).

[60] M. de Oca-Estévez and R. Prosmiti, Front. Chem. **9,** 664693 (2021).

[61] Ch. Jungen, A.L. Roches, and M. Arif, Phil. Trans. R. Soc. Lond. A **355,** 1481 (1997).

[62] Ch. Jungen and A.L. Roches, J. Chem. Phys. **110,** 10784 (1999).

[63] Reference on Constants, Units, and Uncertainty, physics.nist.gov/cuu/constants/index.html, 2019.

[64] Nouredine Zettili, *Quantum mechanics: concepts and applications*. 2nd edition (Wiley, United Kingdom, 2009)

IOP Publishing Journal of Physics B: Atomic, Molecular and Optical Physics
J. Phys. B: At. Mol. Opt. Phys. **56** (2023) 015201 (13pp) https://doi.org/10.1088/1361-6455/aca305

The phenomena of radiative association and charge transfer observed in Ar^++ H and Ar + H^+ collisions

Fatima Talhi[1] **and Moncef Bouledroua**[2,*]

[1] Physics Department, Badji Mokhtar University, B.P. 12, Annaba, Algeria
[2] Laboratoire de Physique des Rayonnements, Badji Mokhtar University, B.P. 12, Annaba 23000, Algeria

E-mail: boulmoncef@netscape.net

Received 31 May 2022, revised 8 November 2022
Accepted for publication 15 November 2022
Published 22 December 2022

Abstract

The aim of the present theoretical work is the characterization of argonium, namely, the molecular ions $^{36}ArH^+$ and $^{38}ArH^+$, revealed in the last decade in the Crab Nebula and the PKS 1823-211 galaxy. The intent is to scrutinize the radiative processes of association, $Ar + H^+ \rightarrow ArH^+$, and charge transfer, $Ar^+ + H \rightarrow Ar + H^+$. To accomplish these two tasks, the corresponding potential-energy curves and dipole moments are chosen to construct the ground and the two first excited ArH^+ molecular states. Once all the required ArH^+ curves are well established and their physical and spectroscopic values are contrasted with previous published data, the cross sections, for the formation of the ionic dimer ArH^+ by radiative association and for the radiative charge transfer in the $Ar^+ + H$ collisions, are computed quantum-mechanically at lower and higher energies. Finally, the temperature-dependent rate coefficients are calculated, and the numerical results are discussed and fitted to a selected analytical expression.

Keywords: argonium potential-energy curves, radiative association, radiative charge transfer, ArH^+ rate coefficients

1. Introduction

Interstellar clouds are basically an accumulation of dust, gas, and plasma. In most of the diffuse clouds where, in particular, ions and neutrals approach each other mutually, the dominant phenomena, namely, the radiative associations (RA), non-radiative and radiative charge transfers (RCTs), and dissociative charge exchanges, may occur at different temperatures and densities. In recent years, astronomers have detected atoms and ions of noble gases in interstellar mediums (ISMs) [1–5]. Such inert elements must have experienced a hard time reacting with other species in space but, until now, only a very few diatomic hydride cations have been detected in extragalactic mediums [6, 7].

Using the European Space Agency's Herschel Space Observatory, Barlow *et al* [1] reported the detection of traces of the protonated argon cation $^{36}ArH^+$, also known as argonium, in the Crab Nebula. The finding was the first noble gas molecule detected in the extra space, where the authors identified two $^{36}ArH^+$ emission lines: one at 617.5 GHz, arising from the rotational line $J = 1 \leftarrow 0$, and a second at 1234.6 GHz, arising from the rotational line $J = 2 \leftarrow 1$. Besides, Schilke *et al* [2] noticed that the unspecified 617.5 GHz absorption transition observed in almost purely atomic diffuse gas was indeed due to argonium $^{36}ArH^+$. Following this, features of $^{38}ArH^+$ were determined as a consequence, and it was proposed that argonium is prevalent in the interstellar medium [2]. Barlow and his coworkers suggested that ArH^+ is primarily formed from the chemical reaction of Ar^+ with molecular hydrogen H_2 $\left(Ar^+ + H_2 \rightarrow ArH^+ + H\right)$, which is further annihilated by the reaction with H_2 $\left(ArH^+ + H_2 \rightarrow Ar + H_3^+\right)$ [8].

Moreover, this rare gas hydride cation has also been detected for the first time in the galaxy PKS 1823-211 by Müller *et al* [9]. In particular, they observed the $J = 1 \leftarrow 0$ transition of $^{36}ArH^+$ at the frequency $617\,525.23 \pm 0.15$ MHz and of

* Author to whom any correspondence should be addressed.

$^{38}ArH^+$ at 616 648.76 ± 0.08 MHz. Their observations led the authors to estimate an argonium presence with the isotopic ratio $^{36}ArH^+/^{38}ArH^+ = 3.46 \pm 0.16$. Müller and his collaborators even believe that ArH^+ may constitute a very good tracer of the almost purely atomic diffuse ISM [9]. Finally, it is worth noting that, unlike its composition on Earth, where ^{40}Ar dominates, the spectral analysis of the argon ISM showed preponderance of ^{36}Ar at 84.6% and ^{38}Ar at 15.4%, with minute traces of ^{40}Ar at 0.025% [2]. Since then, these astronomical discoveries have relaunched a great amount of theoretical and experimental investigations dealing with the ionic dimer ArH^+ and its isotopologues [10–15].

In this work we therefore propose to theoretically examine two molecular processes in which argonium is involved. The first process is the RA of argon atoms, ^{36}Ar or ^{38}Ar, with ionic hydrogen H^+ to form the molecular ion ArH^+. The second process we shall look at is RCT, also known as *charge exchange*. In this process, when the proton H^+ is colliding with the atomic argon, the positive charge is transferred from the ion H^+ to the neutral atomic argon to get the exit channel $Ar^+ + H$. Both ArH^+ radiative reactions are accompanied with emission of photons. We will further compute the corresponding rate coefficients and analyze their behavior with temperature. To do so, we have to primarily construct the most reliable adiabatic ground and excited molecular potentials, via which the concerned species interact, and the permanent and transition dipole moments (TDMs).

Throughout this paper, all the physical formulas and data values are expressed in atomic units (a.u.), unless otherwise specified.

2. Theory

In this section, we briefly outline the quantum-mechanical theories of the RA and RCT phenomena. They are both responsible for the *free-bound* transitions that form the argonium cations ArH^+ and the charge exchange between argon and hydrogen atoms during their ion–atom interactions and collisions.

Here, we adopt the notation of simple prime ($'$) for the *upper* states and double prime ($''$) for the *lower* states.

2.1. Radiative association

RA is defined as the molecular formation process through which two smaller atomic or ionic species collide to form a larger molecule. Such a process should make a substantial contribution to the formation of interstellar neutral and charged molecules, which may eventually be observed in any astrophysical environment.

Accordingly, the RA of argon atoms Ar and hydrogen ions H^+ to form the argon hydride ArH^+ cation is performed via one or both of the following reactions, assumed to be responsible for the formation of ArH^+ molecules:

(a) $X^1\Sigma^+ \leftarrow X^1\Sigma^+$ transitions:

$$\begin{aligned} \mathrm{Ar}\left(^1S\right) + \mathrm{H}^+ &\longrightarrow \mathrm{ArH}^+\left(X^1\Sigma^+\right) \\ &\longrightarrow \mathrm{ArH}^+\left(X^1\Sigma^+\right) + h\nu; \end{aligned} \tag{I-1}$$

(b) $X^1\Sigma^+ \leftarrow C^1\Sigma^+$ and $X^1\Sigma^+ \leftarrow D^1\Pi$ transitions:

$$\begin{aligned} \mathrm{Ar}\left(^{1,3}P\right) + \mathrm{H}^+ &\longrightarrow \left\{ \begin{array}{l} \mathrm{ArH}^+\left(C^1\Sigma^+\right) \\ \mathrm{ArH}^+\left(D^1\Pi\right) \end{array} \right\} \\ &\longrightarrow \mathrm{ArH}^+\left(X^1\Sigma^+\right) + h\nu. \end{aligned} \tag{I-2}$$

All these possible rotational–vibrational transitions, from higher *free* molecular levels towards lower *bound* rovibrational molecular levels, are spontaneously accompanied with emission of photons of energy $h\nu$ and frequency ν.

The *quantal* energy-dependent RA cross sections $Q_a(\epsilon')$ that are effective in association are determined using the expression [16, 17]

$$Q_a(\epsilon') = \frac{64\pi^5}{3c^3k^2} \sum_{J''=0}^{J_{max}} \sum_{v''=0}^{v_{max}} \nu^3 \left[J' M^2_{v''J'\Lambda'',\epsilon'J'-1\Lambda'} + (J'+1) M^2_{v''J'\Lambda'',\epsilon'J'+1\Lambda'}\right], \tag{1}$$

where $k = \sqrt{2\mu\epsilon}/\hbar$ is the wave number of the colliding particles of reduced mass

$$\mu = \frac{M_{Ar} M_H}{M_{Ar} + M_H - m_e}, \tag{2}$$

where ϵ is the energy of the initial free state, and v and J are the vibrational and rotational quantum numbers, respectively. In equation (1), the transition matrix elements $M_{v''J''\Lambda'',\epsilon'J'\Lambda'}$ are taken between the *higher free* states $(\epsilon'J'\Lambda')$ and the *lower bound* states $(v''J''\Lambda'')$, where Λ is the axial component of the electronic angular momentum, which takes the values $\Lambda = 0$ for the Σ molecular states and $\Lambda = 1$ for the Π molecular states. The remaining parameters have their usual meanings.

One should mention that these matrix elements are determined by making use, in both processes (I-1) and (I-2), of the permanent and TDMs $d(R)$ and $D(R)$, respectively. The mean cross sections $\overline{Q}_a(\epsilon')$ in connection with RA can thus be accurately determined using the statistical weight w of the involved molecular transitions, which obtains the values $w = 1/2$ for the $X \leftarrow X$ transitions, $w = 1/6$ for the $X \leftarrow C$ transitions, and $w = 2/6$ for the $X \leftarrow D$ transitions, i.e.

$$\overline{Q}_a(\epsilon') = \frac{1}{2} Q_a(X \leftarrow X) + \frac{1}{6} Q_a(X \leftarrow C) + \frac{2}{6} Q_a(X \leftarrow D). \tag{3}$$

2.2. Radiative charge transfer

The RCT reaction is observed when an ion collides with a neutral atom in which the ionic charge is transferred to the

atom. This process occurs in particular with the ionic ArH^+ system during the collision from the $A\,^1\Sigma^+$ and $B\,^1\Pi$ rotational *continuum* states to the rotational continuum of the ground state $X\,^1\Sigma^+$

$$Ar^+\left(^2P\right)+H\left(^2S\right)\longrightarrow Ar\left(^1S\right)+H^+ + h\nu. \qquad \text{(II)}$$

The energy $h\nu$ of the released photon is given by the expression

$$h\nu=\epsilon'-\epsilon''+\mathcal{E}_{tr}, \tag{4}$$

where ϵ' is the initial free energy of the relative motion of the colliding system, ϵ'' is its final free energy, and $\mathcal{E}_{tr}=V'(\infty)-V''(\infty)$ is the transition energy. If $k^{'}$ and $k^{''}$ are, respectively, the *entrance* and *exit* wave numbers defined as

$$\begin{cases} k'=\sqrt{2\mu\left[\epsilon'-V'(\infty)\right]} \\ k''=\sqrt{2\mu\left[\epsilon''-V''(\infty)-h\nu\right]}, \end{cases} \tag{5}$$

the quantal cross section for the present process (II) is given by [18, 19]

$$\frac{d}{d\epsilon''}Q_c(\epsilon',\epsilon'')=\frac{8}{3}\left(\frac{\pi}{k'}\right)^2(\epsilon'-\epsilon''+\mathcal{E}_{tr})^3\sum_{J'}\left[J'M^2_{J',J'-1}+(J'+1)M^2_{J',J'+1}\right]. \tag{6}$$

Here, $M_{J',J''}$ are the transition matrix elements

$$M_{J',J''}=\int_0^\infty \psi'_{J'}(R)\,D(R)\,\psi''_{J''}(R)\,dR, \tag{7}$$

where $\psi'_{J'}(R)$ and $\psi''_{J''}(R)$ are the upper and lower free wave functions, respectively, $J^{'}$ is the *initial* rotational angular momentum quantum number, and $J''=J'\pm1$ is the *final* rotational quantum number. The total cross section for RCT $Q_c(\epsilon')$ at energy ϵ' is obtained by integrating equation (6) over ϵ''

$$Q_c(\epsilon')=\int_0^\infty \frac{d}{d\epsilon''}Q_c(\epsilon',\epsilon'')\,d\epsilon''. \tag{8}$$

One should finally note that the total cross sections $\overline{Q}_c(\epsilon')$ that are effective in RCT are in fact the mean value computed by the statistically weighted sum

$$\overline{Q}_c(\epsilon')=\frac{1}{3}Q_c(X\leftarrow A)+\frac{2}{3}Q_c(X\leftarrow B). \tag{9}$$

2.3. Rate coefficients

The full quantum-mechanical description of the RA and RCT mechanisms implies the computation of the temperature-dependent rate coefficients [20]

$$\alpha(T)=\left(\frac{8}{\pi\mu}\right)^{1/2}\left(\frac{1}{k_BT}\right)^{3/2}\int_0^\infty \overline{Q}(\epsilon')\,\epsilon'\exp\left(-\frac{\epsilon'}{k_BT}\right)d\epsilon', \tag{10}$$

where k_B is the Boltzmann constant and T is the gas absolute temperature. This integral (10), performed over the Maxwellian velocity distribution, computes the mean of the energy-dependent RA and RCT cross sections, $\overline{Q}_a(\epsilon')$ and $\overline{Q}_c(\epsilon')$.

3. Potential and moment constructions

The transition matrix elements $M_{J',J''}=\langle\psi'_J(R)|\,\xi(R)\,|\psi''_J(R)\rangle$ that appear in equations (1) and (6) are needed in the computation of the RA and RCT cross sections, and thus the rate coefficients. The radial wave functions $\psi_J(R)$ and the permanent and TDMs $\xi(R)\equiv d(R)$ and $\xi(R)\equiv D(R)$ have to be known. The wave functions $\psi'_J(R)$ and $\psi''_J(R)$ are obtained from the numerical resolution of the radial wave equation

$$\frac{d^2\psi_J(R)}{dR^2}+2\mu\left[\epsilon-V(R)-\frac{J(J+1)-\Lambda^2}{2\mu R^2}\right]\psi_J(R)=0. \tag{11}$$

The wave functions are particularly energy normalized with $\epsilon>0$ for the continuum free states and space normalized with $\epsilon<0$ for the *discrete* bound states.

Over the last few decades, a great number of theoretical and experimental investigations have dealt with argonium spectroscopy and the computation of the ArH^+ potentials and moments [21–26]. But the most recent and reliable calculations were performed by Stolyarov and Child [27] in 2005 and Alekseyev *et al* [28] in 2007. All the following argonium electronic potential curves and the involved permanent and TDMs are borrowed exclusively from the *ab initio* data points computed in [27].

3.1. Potential-energy curves

All the possible RA and RCT transitions considered here occur towards the singlet molecular state $X\,^1\Sigma^+$. This requires one to deal only with the first two excited molecular singlet states. Therefore, the involved five electronic potential curves are the following: (a) the ground $X\,^1\Sigma^+$, which dissociates asymptotically into $Ar\left(^1S\right)+H^+$; (b) the first ArH^+ excited set is made of the molecular states $A\,^1\Sigma^+$ and $B\,^1\Pi$, which dissociate asymptotically into $Ar^+\left(^2P^\circ\right)+H\left(^2S\right)$; and (c) the second ArH^+ excited set is made of the molecular states $C\,^1\Sigma^+$ and $D\,^1\Pi$, which dissociate asymptotically into $Ar\left(^{1,3}P\right)+H^+$. Both excited molecular sets lie beyond the ground dissociation limit by about 0.071 and 0.427 a.u., respectively.

Practically, the adopted Stolyarov data points, taken in the interval $R_s\leqslant R\leqslant R_l$, are shifted in all cases so that they smoothly connect with the respective following short- and long-range analytical forms

Table 1. Short-range constant parameters (in a.u.) that appear in the Born–Meyer potentials (12).

	Short range	
Molecular state	α	β
$X^1\Sigma^+$	62.35	3.635
$A^1\Sigma^+$	59.77	3.419
$B^1\Pi$	60.55	3.456
$C^1\Sigma^+$	61.06	3.527
$D^1\Pi$	61.48	3.548

Table 2. A compilation of the static multipolar polarizabilities of ground hydrogen and argon (in a.u.). The adopted quadrupolar and octupolar polarizabilities are marked with $*$.

System	C_d	C_q	C_o	References
Ar^+ in H	4.50	15.0*	131.25*	[33]
	4.475	14.93	130.8	[34]
H^+ in Ar	11.062	51.862	536.38	[35]
	11.143	51.844	534.85	[36]
	11.08	52.80*	536.4*	[37]

* the adopted quadrupolar and octupolar polarizabilities.

$$V(R) \sim \begin{cases} +\alpha \exp(-\beta R) & \text{for } R \leqslant R_s \\ -\dfrac{1}{2}\left(\dfrac{C_d}{R^4} + \dfrac{C_q}{R^6} + \dfrac{C_o}{R^8}\right) & \text{for } R \geqslant R_l, \end{cases} \tag{12}$$

where α and β are the Born–Meyer constant parameters, to be determined for each ArH^+ molecular state, and C_d, C_q, and C_o are, respectively, the static electric *dipole, quadrupole,* and *octupole* polarizabilities of the involved neutral species, namely, H or Ar. Numerically, the cubic spline method yields the parameters α and β listed in table 1. Furthermore, we have adopted, for the dominant R^{-4} term of the long-range potential (12), the polarizability values proposed by NIST, i.e. $C_d = 4.50$ for hydrogen and $C_d = 11.23$ for argon [29]. Both data are comparable with the recommended values, $4.504\,56 \pm 0.000\,03$ and 11.083 ± 0.007 from Schwerdtfeger and Nagle [30], and with the measured values $C_d = 4.499\,74$ of Miller and Bederson [31] and $C_d = 11.229\,23$ of Olney *et al* [32], respectively. Some additional published higher-order multipolar polarizabilities are compiled in table 2, and the adopted values of the quadrupole and octupole polarizabilities are from [33, 37].

Figure 1 displays the five ArH^+ adiabatic PECs, as constructed above. Since all the RA and RCT transitions involve the final ground state $X^1\Sigma^+$, it is therefore of primary interest to suitably construct this curve and ensure its good quality with the highest accuracy. Tables 3 and 4 provide the spectroscopic parameters and the *rotationless–vibrational* energy levels of the ArH^+ molecular states, and, when possible, the data are compared with published values. All the higher potential curves are monotonically decreasing towards the $Ar^+\left(^2P^\circ\right) + H\left(^2S\right)$ and $Ar\left(^{1,3}P\right) + H^+$ dissociation limits, and the curves $C^1\Sigma^+$ and $D^1\Pi$ exhibit two *humps* in the vicinity of $R \sim 3-5$ a.u. Moreover, the ground state potential $X^1\Sigma^+$ can hold up to 27 rotationless-vibrational levels, whereas the first and second excited potential sets are remarkably very shallow. The rovibrational data are listed in table 5 for both isotopic dimers $^{36}ArH^+$ and $^{38}ArH^+$, and the results are compared with published values whenever available. The particular ArH^+ rotational $1-0$ and $2-1$ lines are listed in table 6 and compared with other published values. The discrepancies with the present results, shown in table 6, are not important. More specifically, Barlow *et al* [1] measured the rotational frequencies 617.5 and 1234.6 GHz for the line transitions $^{36}ArH^+$ $(J = 1 \leftarrow 0)$ and $^{36}ArH^+$ $(J = 2 \leftarrow 1)$, respectively. All the values show there is satisfaction with the present ArH^+ potential constructions.

3.2. Permanent and transition dipole moments

To perform the required RA and RCT calculations, one has to construct besides the permanent dipole moment (PDM) $d(R)$ and the TDMs $D(R)$. The former moment is essentially needed to deal with the $X \leftarrow X$ free-bound transitions. More precisely, we adopted, over the internuclear interval $0 \leqslant R \leqslant 12$, the calculated PDM data points from Stolyarov and Child [27], which we extended in the long-range region using the formula [43, 44]

$$d(R) \sim \frac{R}{2} - \frac{2C_d}{R^2}. \tag{13}$$

In addition, the TDMs are constructed from the data points generated in [27]. They concern the quantum-mechanically allowed molecular transitions from the ArH^+ excited states $A^1\Sigma^+$, $B^1\Pi$, $C^1\Sigma^+$, and $D^1\Pi$ towards the ArH^+ ground state $X^1\Sigma^+$. They are extended, in the long-range regions, with the

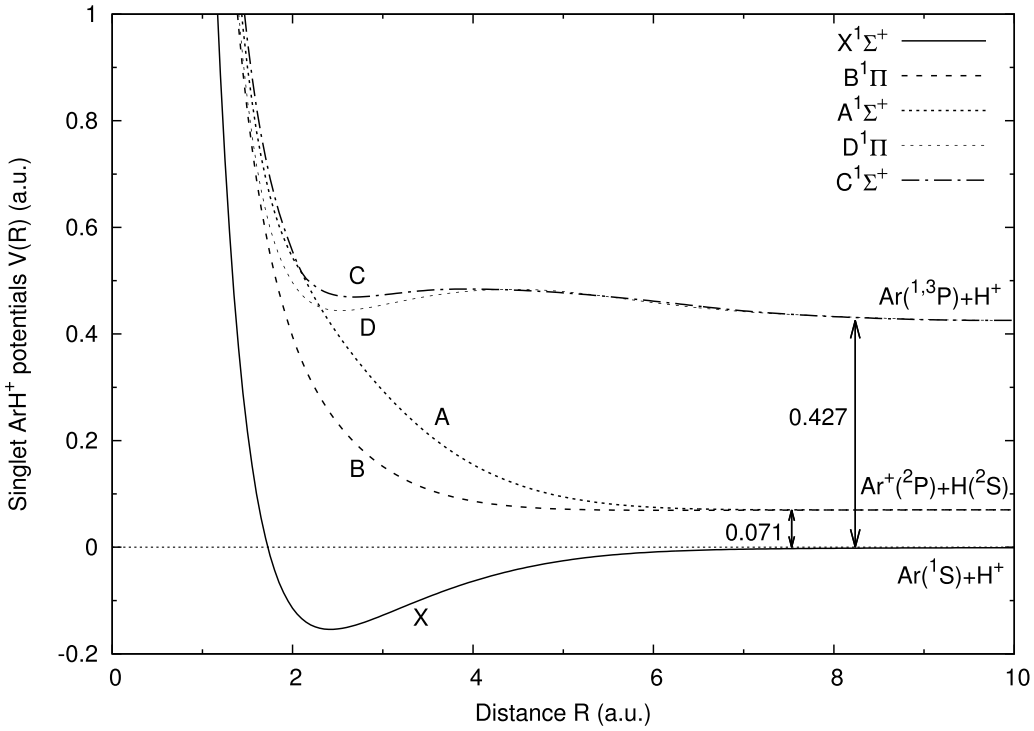

Figure 1. ArH^+ potential-energy curves, as constructed from the Stolyarov and Child data points [27].

Table 3. Spectroscopic data of the constructed ArH^+ potentials.

Molecular state	Equilibrium distance R_e (Å)	Well depth $-D_e$ (cm^{-1})	Hump h (cm^{-1})	References
$X^1\Sigma^+$	1.277	33 779.3		
	1.279	33 391.36		[27]
	1.268	34 608.4		[28]
	1.286	31 374.97		[38]
	1.244 ± 0.003	$33\,375.37 \pm 432.77$		[39]
	1.280	32 460		[40]
$A^1\Sigma^+$	4.286	31.0457		
$B^1\Pi$	3.285	192.049		
$C^1\Sigma^+$	5.172	761.211	123.708	
$D^1\Pi$	5.204	722.278	123.706	

Table 4. Rotationless-vibrational energy levels of argonium $^{36}ArH^+$ in units of cm^{-1}.

v	$X^1\Sigma^+$	$A^1\Sigma^+$	$B^1\Pi$	$C^1\Sigma^+$	$D^1\Pi$
0	−32 424.701	−61.363	−187.036	−779.221	−739.390
1	−29 809.441	−13.703	−78.705	−462.728	−421.639
2	−27 313.744	−1.574	−23.275	−181.909	−145.584
3	−24 934.848		−3.791		
4	−22 669.965				
5	−20 516.329				
13	−7014.710				
15	−4647.520				
20	−790.945				
25	−13.112				
26	−2.637				

Table 5. Rotational–vibrational states relative to both argonium isotopes $^{36}ArH^+$ and $^{38}ArH^+$ in units of cm^{-1}.

v	J	$^{36}ArH^+$	$^{38}ArH^+$	References	
0	0	−32424.701	−32425.663	31101 ± 242	[41]
				32066.48	[42]
0	5	−32115.987	−32117.386		
1	0	−29809.441	−29812.189	28536 ± 242	[41]
				29471.34	[42]
1	7	−29255.304	−29258.819		
2	8	−26628.733	−26634.027		
3	10	−23930.705	−23937.854		
5	20	−17050.469	−17062.994		

Table 6. Computed and measured rotational lines for $J = 1 - 0$ and $J = 2 - 0$ of $^{36}ArH^+$ and $^{38}ArH^+$ in MHz.

Transition	$^{36}ArH^+$	$^{38}ArH^+$	References
$J = 1 \leftarrow 0$	617704.99	16828.47	
	617525.226 ± 0.151	616648.762 ± 0.083	[3]
	617525.23 ± 0.15	616648.76 ± 0.08	[9]
	617525.149 ± 0.020	616648.707 ± 0.020	[12]
$J = 2 \leftarrow 1$	1234969.74	1233217.96	
	1234602.75 ± 0.30	1232851.00 ± 0.04	[9]

analytical form $D(R) \sim -p/R^n$, where p and n are constants to be determined for each transition, and are supposed to behave linearly in the short-range regions. Both the PDMs and TDMs are respectively plotted in figures 2(a) and (b).

Once the potentials and the permanent and TDMs are well established, we numerically solve the radial wave equation (11) to get the free and bound wave functions and the corresponding energies, which should allow us to compute the matrix elements using equation (7).

3.3. Radiative lifetime

Supposing the approximations $J = J' \simeq J''$, the radiative lifetime of each rovibrational level is $\tau = 1/\mathcal{A}(vJ\Lambda)$, with the total spontaneous emission rates being given by

$$\mathcal{A}(v'J\Lambda') = \frac{32}{3}\left(\frac{\pi}{c}\right)^3 \frac{2-\delta_{0,\Lambda'+\Lambda''}}{2-\delta_{0,\Lambda'}} \times \left[\int_0^\infty \nu^3_{v'J\Lambda',\epsilon''J\Lambda''} M^2_{v'J\Lambda',\epsilon''J\Lambda''} d\epsilon'' + \sum_{v''} \nu^3_{v'J\Lambda',v''J\Lambda''} M^2_{v'J\Lambda',v''J\Lambda''}\right]. \quad (14)$$

The upper and lower states, defined by the quantum numbers $(v'J'\Lambda')$ and $(v''J''\Lambda'')$, are related to the *bound-free* and *bound–bound* transitions, respectively.

First, it is important to note that the excited $A\,^1\Sigma^+$ and $B\,^1\Pi$ PECs are almost entirely repulsive over the whole range of separation distances, and table 4 confirms this ascertainment. This is not the case for the excited $C\,^1\Sigma^+$ and $D\,^1\Pi$ potentials. Indeed, although these two molecular states are very shallow, they are both able to hold a very limited number of rovibrational levels. It is thus possible to compute the individual radiative lifetimes of the upper states involved in the transitions $X\,^1\Sigma^+ \leftarrow C\,^1\Sigma^+$ and $X\,^1\Sigma^+ \leftarrow D\,^1\Pi$ towards the deeper lower ground state $X\,^1\Sigma^+$. Table 7 lists the individual lifetimes of the upper molecular C and D states. Such values may serve as a good probe in the evaluation of the accuracy of the ArH^+ potential sets.

The mean lifetime $\overline{\tau}$ is counted with

$$\frac{1}{\overline{\tau}} = \frac{1}{3}\mathcal{A}_{X\leftarrow C}(v'_{\max}00) + \frac{2}{3}\mathcal{A}_{X\leftarrow D}(v'_{\max}01), \quad (15)$$

in which the calculations imply the highest rotationless–vibrational states that are both in the vicinity of the dissociation limit. From table 7, the present calculations lead to $\overline{\tau} \simeq 2.88$ ns.

4. Results and discussion

Once the needed ArH^+ potential curves and permanent and TDNs are well established and have demonstrated their reliability and consistency, we proceed into the quantal computation of the RA and charge transfer cross sections, namely, $Q_a(\epsilon)$ and $Q_c(\epsilon)$, both provided in terms of the energy in equations (1) and (8), respectively. From there, we should be able to calculate the temperature-dependent rate coefficients $\alpha(T)$ and determine their respective variation laws with T.

The calculated $X\,^1\Sigma^+ \leftarrow X\,^1\Sigma^+$ energy-dependent cross sections $Q_a(\epsilon)$, effective in the ArH^+ RA, are displayed in figure 3(a) for two isotopologues, $^{36}ArH^+$ and $^{38}ArH^+$. From these plots, one may notice the perfect match in the position

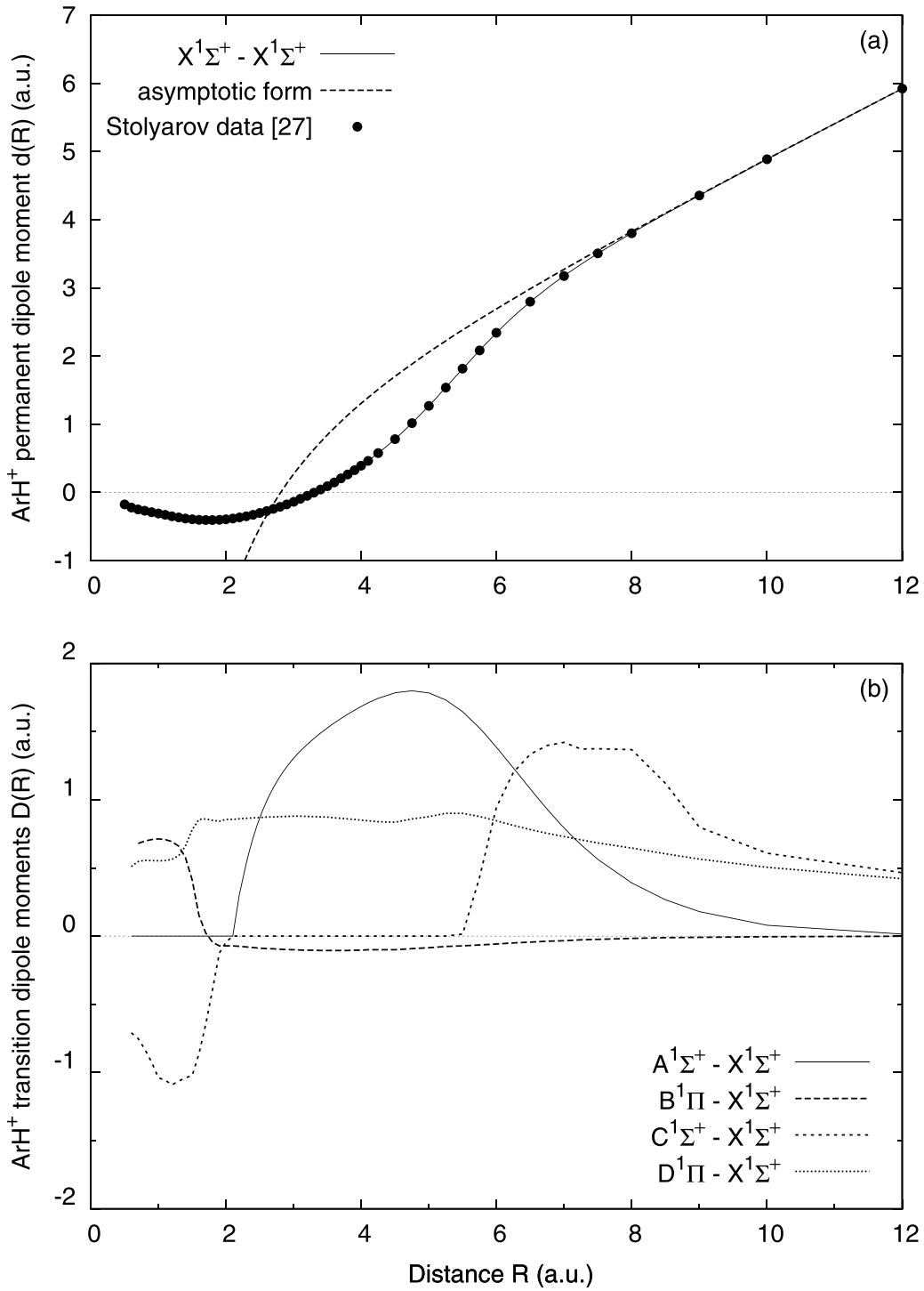

Figure 2. (a) The ArH^+ PDM relative to the $X-X$ transition. (b) ArH^+ TDMs in connection with the $X \leftarrow A$, $X \leftarrow B$, $X \leftarrow C$, and $X \leftarrow D$ transitions.

Table 7. A compilation of the lifetime values, in ns, computed for the rovibrational states.

	$C^1\Sigma^+$					$D^1\Pi$				
v	$J=0$	$J=1$	$J=2$	$J=3$	$J=4$	$J=0$	$J=1$	$J=2$	$J=3$	$J=4$
0	9.66	9.69	9.83	10.24	11.06	10.17	10.13	10.11	10.31	10.86
1	3.67	3.60	3.45	3.21	2.85	4.64	4.60	4.47	4.24	3.83
2	2.26	2.26	2.26	2.26	2.28	3.34	3.34	3.35	3.37	3.40

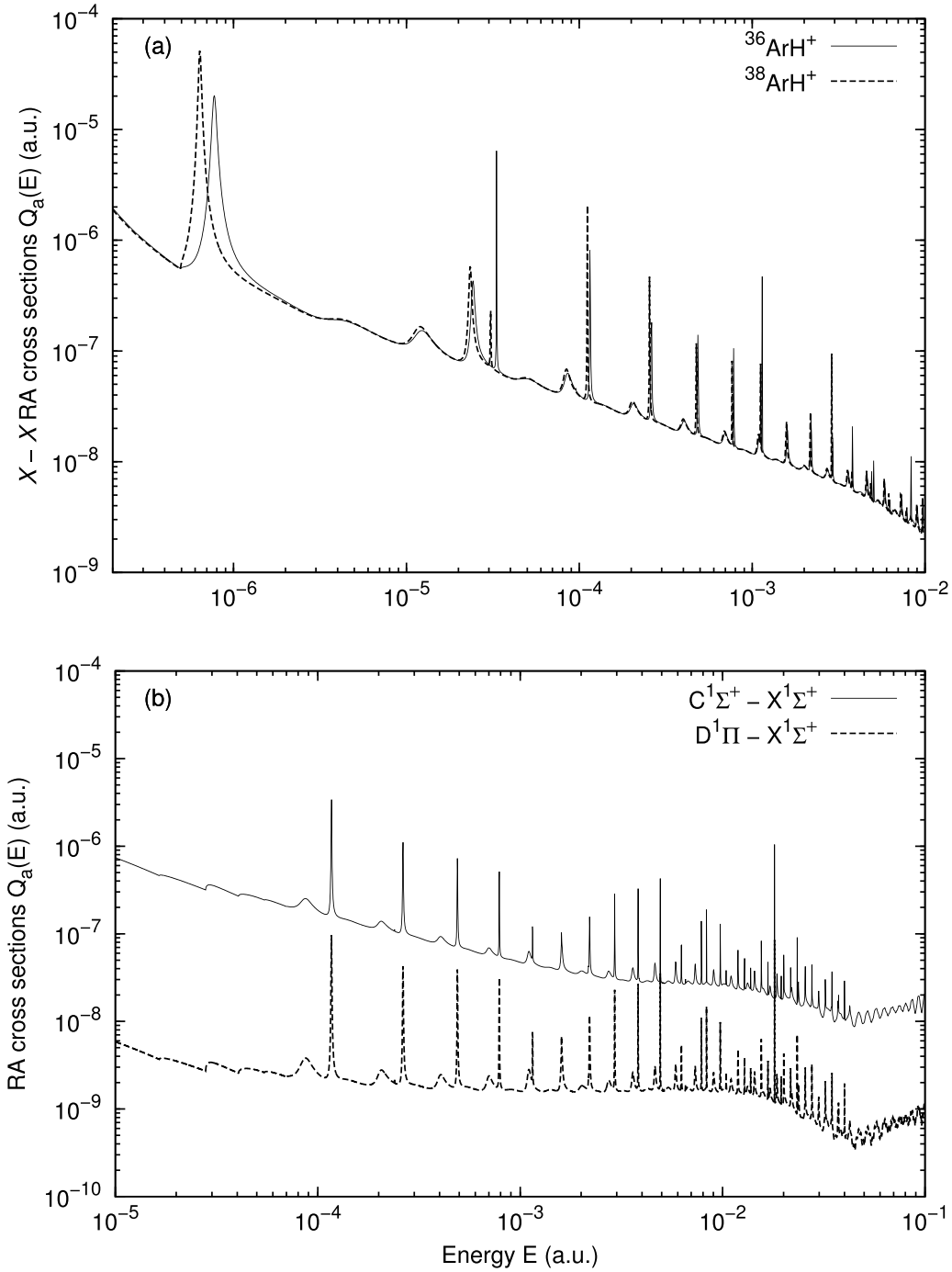

Figure 3. ArH^+ RA cross sections in terms of energy in connection with the (a) $X \leftarrow X$ transitions for both isotopes $^{36}ArH^+$ and $^{38}ArH^+$, and with the (b) $X \leftarrow C$ and $X \leftarrow D$ $^{36}ArH^+$ transitions.

of the resonance peaks, mainly at higher energies, which suggests that the isotopic effects do not significantly affect the general shape of the $X \leftarrow X$ RA cross sections. Furthermore, the computed cross sections $Q_a(\epsilon)$, in connection with the transitions $X \leftarrow C$ and $X \leftarrow D$, are presented in figure 3(b). The $X \leftarrow C$ transitions definitely seem to be the most probable and stronger than those due to the $X \leftarrow D$ transitions. More specifically, the observed resonance structures are mainly due to the quasibound rovibrational levels of the initial states. Due to the smallness of the ArH^+ reduced mass, only a very limited number of resonance peaks can be predicted and have obvious energy positions, which tightly depend on the constructed potentials [45].

Moreover, figure 4 illustrates the RCT cross sections $Q_c(\epsilon)$ rising from the allowed transitions $X \leftarrow A$ and $X \leftarrow B$. As table 4 shows, the involved excited potential curves support

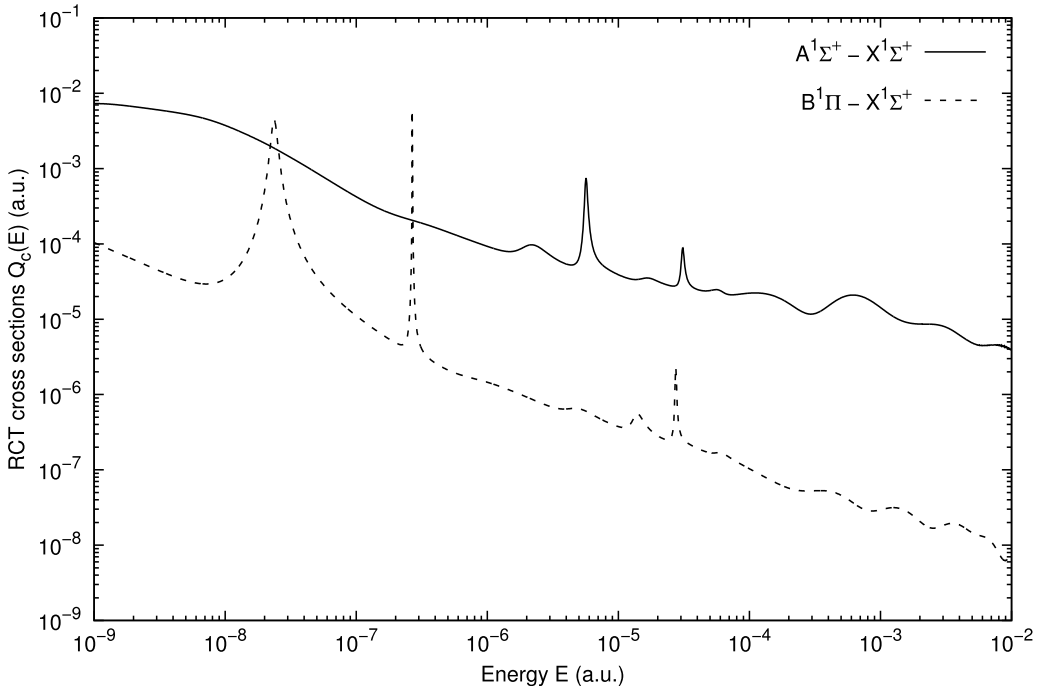

Figure 4. $^{36}ArH^+$ RCT cross sections in terms of energy in connection with the $X \leftarrow A$ and $X \leftarrow B$ transitions.

extremely weak quasibound vibrational states. This may explain the reduced number of the resonance structures in the corresponding cross sections and the dominance of the $X \leftarrow A$ transitions compared to those of $X \leftarrow B$ [46]. At lower collision velocities, the ArH^+ system does not have enough kinetic energy to approach the potential barrier of the ground molecular state $X^1\Sigma^+$. But above the energy 10^{-8} a.u., the system is able to penetrate the potential barrier and the regions where the $X^1\Sigma^+$ state contains a deep attractive well. In this region, there is essentially a sharp rise in the cross sections, and therefore numerous resonance lines appear, which are all caused by the rovibrational quasibound states of the ArH^+ molecule in the $X^1\Sigma^+$ electronic state.

Having now determined the quantal cross sections $Q_a(\epsilon)$ and $Q_c(\epsilon)$, it is hence possible to proceed with the computation of the temperature-dependent rate coefficients that are effective in RA and charge transfer, $\alpha_a(T)$ and $\alpha_c(T)$, respectively. Using equation (10), the RA and RCT rates are computed in the temperature range 10–10 000 K, and the numerical results are compiled in tables 8 and 9. The former table lists the generated $X \leftarrow X$ data for both argon isotopes $^{36}ArH^+$ and $^{38}ArH^+$, whereas the latter presents the RA and RCT results arising from the first and second excited transition sets.

The statistically averaged values of the rate coefficients are further determined using the relationships

$$\alpha_a(T) = \frac{1}{3}\alpha_{X\leftarrow C}(T) + \frac{2}{3}\alpha_{X\leftarrow D}(T) \tag{16}$$

$$\alpha_c(T) = \frac{1}{3}\alpha_{X\leftarrow A}(T) + \frac{2}{3}\alpha_{X\leftarrow B}(T) \tag{17}$$

and are presented in table 9 as well. Before all, we found a paucity of published data that concern argonium RA and charge transfer. Nevertheless, for the sake of comparison, Kraemer *et al* [46] published their graphical results of the rate coefficients $\alpha_a(T)$ for the formation of the ionic dimer ArH^+ in the ground state $X^1\Sigma$. Our graphical estimation from figure 9 of [46] yields, for three particular temperatures, the values $\alpha_a(10) \simeq 5.6 \times 10^{-19}$, $\alpha_a(100) \simeq 3.8 \times 10^{-19}$, and $\alpha_a(1000) \simeq 2.3 \times 10^{-19}$ cm^3 s^{-1}. Although the estimated RA rate coefficients are not exactly the same in this case, the discrepancies are important, but the magnitudes are quite similar.

On the other hand, the lack of published data on ArH^+ RCT forced us rather to compare the present results with those coming from collisions among species belonging to families close to Ar/Ar^+ and H^+/H. Indeed, the RCT rates at $T = 300$ K in connection with interactions of Ar with He^+ and Ne with He^+ yielded the values $\alpha_c(300) \simeq 9.86 \times 10^{-15}$ in Babb and McLaughlin [47] and $\alpha_c(300) \simeq 5 \times 10^{-16}$ cm^3 s^{-1} in Liu *et al* [48], respectively. Our generated weighted value at the same temperature is equal to $\alpha_c(300) \simeq 5.785 \times 10^{-18}$ cm^3 s^{-1}.

The graphical representations of the average RA and RCT rate coefficients are illustrated in figure 5. The upper figure 5(a) represents the statistically weighted average results of the ArH^+ RA rate coefficients, depending on the considered isotopes. The lower figure 5(b) displays the profiles of the average rate coefficients $\alpha_a(T)$ and $\alpha_c(T)$, obtained in terms of temperature. The plots demonstrate that, in the same gaseous environment, the RCT phenomena dominate the RA.

Table 8. The $X - X$ RA rate coefficients (in $cm^3\ s^{-1}$) computed at various temperatures T (in K). The notation $a[-n]$ stands for $a \times 10^{-n}$.

	$X \leftarrow X$	
Temperature T (K)	$^{36}ArH^+$	$^{38}ArH^+$
10	**1.173[−19]**	**1.012[−19]**
50	**9.899[−20]**	**1.018[−19]**
100	**9.825[−20]**	**9.631[−20]**
200	**9.949[−20]**	**9.221[−20]**
300	**9.712[−20]**	**9.027[−20]**
400	**9.397[−20]**	**8.833[−20]**
500	**9.087[−20]**	**8.619[−20]**
600	**8.802[−20]**	**8.398[−20]**
700	**8.543[−20]**	**8.179[−20]**
800	**8.309[−20]**	**7.969[−20]**
900	**8.099[−20]**	**7.769[−20]**
1000	**7.909[−20]**	**7.582[−20]**
2000	**6.810[−20]**	**6.326[−20]**
3000	**6.581[−20]**	**5.814[−20]**
4000	**6.814[−20]**	**5.715[−20]**
5000	**7.263[−20]**	**5.828[−20]**
6000	**7.757[−20]**	**6.019[−20]**
7000	**8.198[−20]**	**6.205[−20]**
8000	**8.542[−20]**	**6.350[−20]**
9000	**8.781[−20]**	**6.442[−20]**
10000	**8.920[−20]**	**6.480[−20]**

Table 9. RA and RCT rate coefficients (in $cm^3\ s^{-1}$) computed at various temperatures T (in K). The notation $a[-n]$ stands for $a \times 10^{-n}$.

	RA rate coefficients			RCT rate coefficients		
Temperature T (K)	$C \rightarrow X$	$D \rightarrow X$	Average	$A \rightarrow X$	$B \rightarrow X$	Average
10	**4.271[−19]**	**4.548[−21]**	**1.454[−19]**	**1.420[−18]**	**1.142[−20]**	**4.811[−19]**
50	**4.019[−19]**	**7.883[−21]**	**1.392[−19]**	**3.466[−18]**	**1.957[−20]**	**1.168[−18]**
100	**3.823[−19]**	**9.794[−21]**	**1.339[−19]**	**7.611[−18]**	**2.751[−20]**	**2.555[−18]**
200	**3.686[−19]**	**1.246[−20]**	**1.312[−19]**	**1.326[−17]**	**4.569[−20]**	**4.452[−18]**
300	**3.712[−19]**	**1.481[−20]**	**1.336[−19]**	**1.723[−17]**	**6.113[−20]**	**5.785[−18]**
400	**3.805[−19]**	**1.693[−20]**	**1.381[−19]**	**2.029[−17]**	**7.329[−20]**	**6.812[−18]**
500	**3.923[−19]**	**1.883[−20]**	**1.433[−19]**	**2.271[−17]**	**8.297[−20]**	**7.626[−18]**
600	**4.051[−19]**	**2.053[−20]**	**1.487[−19]**	**2.468[−17]**	**9.084[−20]**	**8.286[−18]**
700	**4.180[−19]**	**2.205[−20]**	**1.540[−19]**	**2.631[−17]**	**9.737[−20]**	**8.836[−18]**
800	**4.306[−19]**	**2.345[−20]**	**1.592[−19]**	**2.770[−17]**	**1.029[−19]**	**9.302[−18]**
900	**4.430[−19]**	**2.473[−20]**	**1.641[−19]**	**2.890[−17]**	**1.076[−19]**	**9.705[−18]**
1000	**4.548[−19]**	**2.591[−20]**	**1.689[−19]**	**2.995[−17]**	**1.117[−19]**	**1.006[−17]**
2000	**5.390[−19]**	**3.332[−20]**	**2.019[−19]**	**3.636[−17]**	**1.368[−19]**	**1.221[−17]**
3000	**5.718[−19]**	**3.547[−20]**	**2.142[−19]**	**3.996[−17]**	**1.516[−19]**	**1.342[−17]**
4000	**5.832[−19]**	**3.558[−20]**	**2.181[−19]**	**4.271[−17]**	**1.638[−19]**	**1.434[−17]**
5000	**5.875[−19]**	**3.511[−20]**	**2.192[−19]**	**4.511[−17]**	**1.752[−19]**	**1.515[−17]**
6000	**5.883[−19]**	**3.449[−20]**	**2.191[−19]**	**4.736[−17]**	**1.866[−19]**	**1.591[−17]**
7000	**5.860[−19]**	**3.380[−20]**	**2.178[−19]**	**4.954[−17]**	**1.980[−19]**	**1.664[−17]**
8000	**5.806[−19]**	**3.304[−20]**	**2.156[−19]**	**5.170[−17]**	**2.097[−19]**	**1.737[−17]**
9000	**5.724[−19]**	**3.223[−20]**	**2.123[−19]**	**5.386[−17]**	**2.217[−19]**	**1.810[−17]**
10000	**5.619[−19]**	**3.137[−20]**	**2.082[−19]**	**5.604[−17]**	**2.341[−19]**	**1.884[−17]**

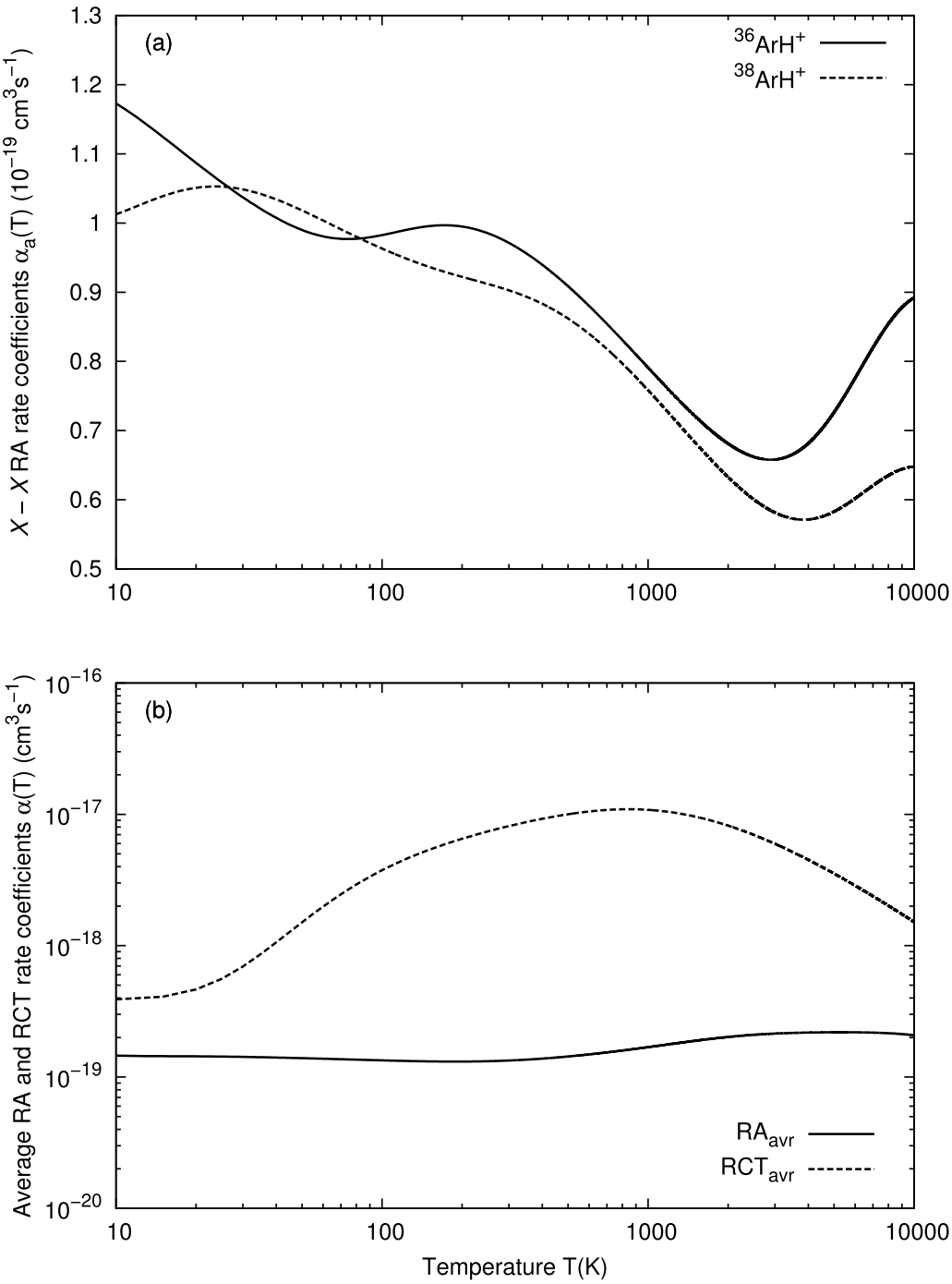

Figure 5. The variation of RA and RCT rate coefficients with temperature. The upper figure (a) displays the isotopic effects on the $X - X$ rate, whereas the lower figure (b) compares the average RA and RCT rates.

The investigation on the $Ne - He^+$ collisions conducted by Liu *et al* [48] concluded that the RA and RCT rate coefficients, in the temperature range 10–10 000 K, are of the same magnitude, whereas the present calculations prove the predominance of the RCT processes over the RA processes.

Finally, the average RA and RCT rate coefficients have both been fitted with the polynomial expression

$$\alpha(T) = \sum_{j=0}^{9} a_j T^j. \tag{18}$$

It becomes apparent that the best fits can be obtained with the first *ten* monomials. For $100 \leqslant T \leqslant 10\,000$ K, the present results are plotted in figures 6 and 7. At higher temperatures, the concordances are specifically better.

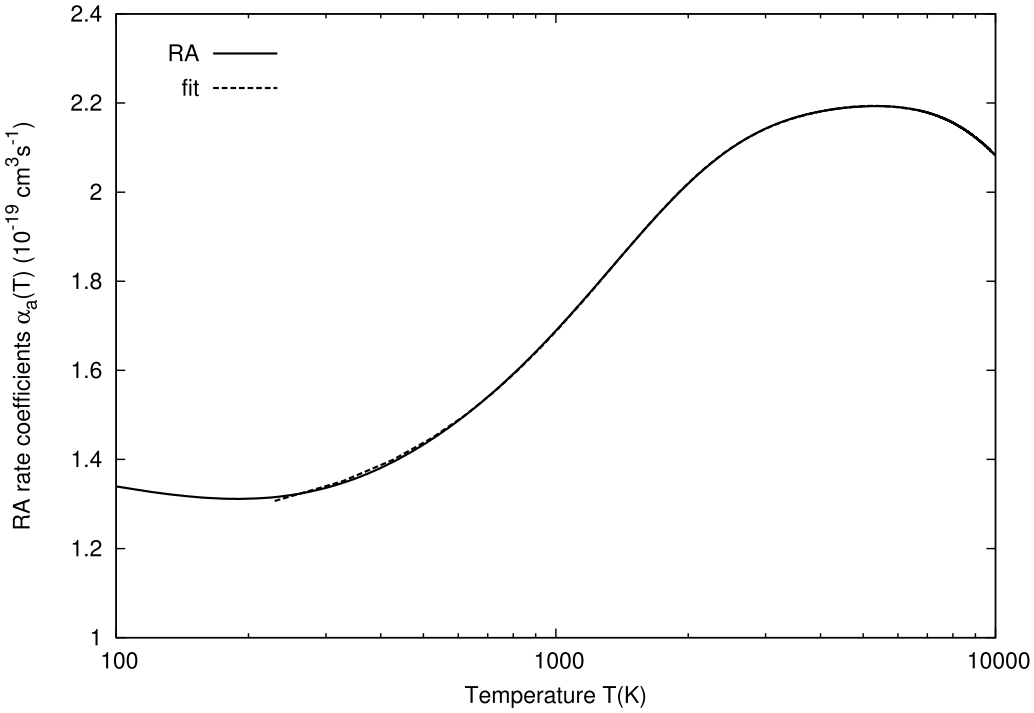

Figure 6. Fitting of the average RA rate coefficients to the polynomial expression given in equation (18).

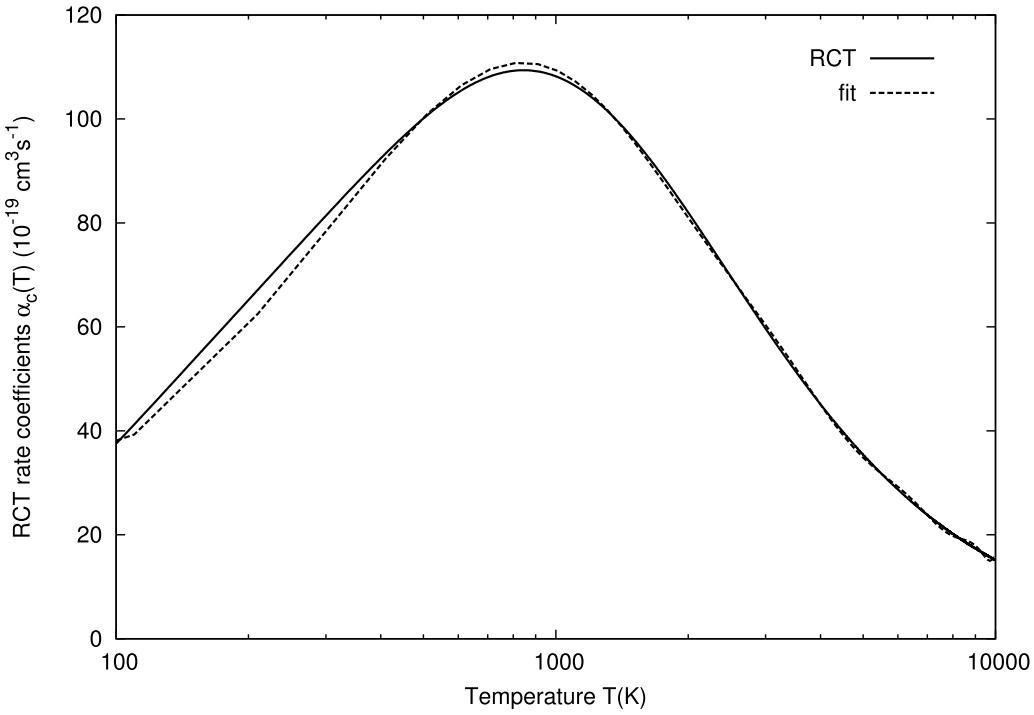

Figure 7. Fitting of the average RCT rate coefficients to the polynomial expression given in equation (18).

5. Conclusion

This work tries to characterize the recently detected argonium molecule ArH^+ in the extragalactic Crab Nebula and PKS 1823-211 galaxy. More specifically, we calculated, over wide energy and temperature ranges, the cross sections and the rate coefficients for the formation of ArH^+ via the RA of Ar^+ with H and the charge exchange between neutral Ar and the proton H^+. The ArH^+ characterization required us to set up the potential curves, through which the involved atomic species interact, and the corresponding permanent and TDMs. The obtained cross sections allowed the computation of the temperature-dependent rate coefficients, which showed predominance of RCT over RA in the temperature interval 10–10 000 K.

Data availability statement

The data generated and/or analysed during the current study are not publicly available for legal/ethical reasons but are available from the corresponding author on reasonable request.

Acknowledgments

One of the authors, M B, would like to thank Dr Kamel Alioua, from the University Mohamed Cherif Messaadia of Souk Ahras, Algeria, for his kind help fulfilling some of the numerical tasks related to this work.

ORCID iD

Moncef Bouledroua https://orcid.org/0000-0002-3924-6767

References

[1] Barlow M J *et al* 2013 *Science* **342** 1343
[2] Schilke P *et al* 2014 *Astron. Astrophys.* **566** A29
[3] Cueto M, Cernicharo J, Barlow M J, Swinyard B M, Herrero V J, Tanarro I and Doménech J L 2014 *Astrophys. J. Lett.* **783** L5
[4] Güsten R, Wiesemeyer H, Neufeld D, Menten K M, Graf U U, Jacobs K, Klein B, Ricken O, Risacher C and Stutzki J 2019 *Nature* **568** 357
[5] Neufeld D A, Goto M, Geballe T R, Güsten R, Menten K M and Wiesemeyer H 2020 *Astrophys. J.* **894** 37
[6] Müller H S P, Schlöder F, Thorwirth S and Winnewisser G 1997 The Cologne database for molecular spectroscopy, CDMS *The Dense Interstellar Medium in Galaxies (Springer Proceedings in Physics* vol 91) ed S Pfalzner, C Kramer, C Straubmeier and A Heithausen (*Berlin*: Springer)
[7] Hamilton J R, Faure A and Tennyson J 2016 *Mon. Not. R. Astron. Soc.* **455** 3281
[8] Priestley F D, Barlow M J and Viti S 2017 *Mon. Not. R. Astron. Soc.* **472** 4444
[9] Müller H S P, Muller S, Schilke P, Bergin E A, Black J H, Gerin M, Lis D C, Neufeld D A and Suri S 2015 *Astron. Astrophys.* **582** L4
[10] Roueff E, Alekseyev A B and Le Bourlot J 2014 *Astron. Astrophys.* **566** A30
[11] Coxon J A and Hajigeorgiou P G 2016 *J. Mol. Spectrosc.* **330** 63
[12] Bizzocchi L, Dore L, Esposti C D and Tamassia F 2016 *Astrophys. J. Lett.* **820** L26
[13] Abdoulanziz A, Colboc F, Little D A, Moulane Y, Zs Mezei J, Roueff E, Tennyson J, Schneider I F and Laporta V 2018 *Mon. Not. R. Astron. Soc.* **479** 2415
[14] Dagdigian P J 2018 *Mon. Not. R. Astron. Soc.* **477** 802
[15] Bastian B, Carrascosa E, Kaiser A, Meyer J, Michaelsen T, Czakób G, Hase W L and Wester R 2019 *Int. J. Mass Spectrom.* **438** 175
[16] Gianturco F A and Gori Giorgi P 1997 *Astrophys. J.* **479** 560
[17] Forrey R C, Babb J F, Courtney E D S, McArdle R T and Stancil P C 2020 *Astrophys. J.* **898** 86
[18] Zhao L B, Stancil P C, Gu J P, Liebermann H-P, Li Y, Funke P, Buenker R J, Zygelman B, Kimura M and Dalgarno A 2004 *Astrophys. J.* **615** 1063
[19] Lin X, Peng Y, Wu Y, Wang J, Janev R and Shao B 2017 *Astron. Astrophys.* **598** A75
[20] Antipov S V, Gustafsson M and Nyman G 2013 *Mon. Not. Roy. Astron. Soc.* **430** 946
[21] Schutte C J H 2001 *Chem. Phys. Lett.* **345** 525
[22] Schutte C J H 2001 *Chem. Phys. Lett.* **350** 181
[23] Schutte C J H 2002 *Chem. Phys. Lett.* **353** 389
[24] Coxon J A and Molski M 2004 *J. Mol. Spectrosc.* **223** 51
[25] Kirrander A, Child M S and Stolyarov A V 2006 *Phys. Chem. Chem. Phys.* **8** 247
[26] de Oca-Estévez M and Prosmiti R 2021 *Front. Chem.* **9** 664693
[27] Stolyarov A V and Child M S 2005 *Phys. Chem. Chem. Phys.* **7** 2259
[28] Alekseyev A B, Liebermann H-P and Buenker R J 2007 *Phys. Chem. Chem. Phys.* **9** 5088
[29] NIST Chemistry Webook 2022 NIST standard reference database number 69 (Gaithersburg, MD: National Institute of Standards and Technology)
[30] Schwerdtfeger P and Nagle J K 2018 *Mol. Phys.* **117** 1200
[31] Miller M and Bederson B 1977 *Adv. At. Mol. Phys.* **13** 1
[32] Olney T N, Cann N M, Cooper G and Brion C E 1997 *Chem. Phys.* **223** 59
[33] Tang K T, Norbeck J M and Certain P R 1976 *J. Chem. Phys.* **64** 3063
[34] Figari G, Musso G F and Magnasco V 1983 *Mol. Phys.* **50** 1173
[35] Thakkar A J, Hettema H and Wormer P E S 1992 *J. Chem. Phys.* **97** 3252
[36] Spelsberg D and Meyer W 1996 *J. Phys. Chem.* **100** 14637
[37] Mitroy J and Zhang J-Y 2007 *Phys. Rev.* A **76** 032706
[38] Rosmus P 1979 *Theor. Chim. Acta* **51** 359
[39] Hotop H, Roth T E, Ruf M-W and Yencha A J 1998 *Theor. Chem. Acc.* **100** 36
[40] Maltsev M A Morozov I V and Osina E L 2019 *High Temp.* **57** 335
[41] Lorenzen J, Hotop H, Ruf M W and Morgner H 1980 *Z. Phys.* A **297** 19
[42] Hirst D M, Guest M F and Rendell A P 1992 *Mol. Phys.* **77** 279
[43] Jungen C, Roches A L and Arif M 1997 *Phil. Trans. R. Soc.* A **355** 1481
[44] Jungen C and Roches A L 1999 *J. Chem. Phys.* **110** 10784
[45] da Silva H Jr, Raoult M, Aymar M and Dulieu O 2015 *New J. Phys.* **17** 045015
[46] Kraemer W P, Juřek M and Špirko V 1997 Quantum-mechanical studies of radiative sssociation reactions: formation of HeH^+, NeH^+ and ArH^+ *Vibration-Rotational Spectroscopy and Molecular Dynamics (Advanced Series in Physical Chemistry* vol 9*)* ed D Papousek (Singapore: World Scientific) pp 516–53
[47] Babb J and McLaughlin B M 2018 *Astrophys. J.* **860** 151
[48] Liu X J, Qu Y Z, Xiao B J, Liu C H, Zhou Y, Wang J G and Buenker R J 2010 *Phys. Rev.* A **81** 022717